



HAL
open science

Variable kinematics finite plate elements for the buckling analysis of sandwich composite panels

G. Di Cara, M. D'ottavio, O. Polit

► **To cite this version:**

G. Di Cara, M. D'ottavio, O. Polit. Variable kinematics finite plate elements for the buckling analysis of sandwich composite panels. *Composite Structures*, 2023, pp.117856. 10.1016/j.compstruct.2023.117856 . hal-04372354

HAL Id: hal-04372354

<https://hal.science/hal-04372354>

Submitted on 4 Jan 2024

HAL is a multi-disciplinary open access archive for the deposit and dissemination of scientific research documents, whether they are published or not. The documents may come from teaching and research institutions in France or abroad, or from public or private research centers.

L'archive ouverte pluridisciplinaire **HAL**, est destinée au dépôt et à la diffusion de documents scientifiques de niveau recherche, publiés ou non, émanant des établissements d'enseignement et de recherche français ou étrangers, des laboratoires publics ou privés.

Variable kinematics finite plate elements for the buckling analysis of sandwich composite panels

G. Di Cara^{a,1}, M. D'Ottavio^a, O. Polit^a

*^aLaboratoire Energétique Mécanique Electromagnétisme – EA 4416
Université Paris Nanterre
50, rue de Sèvres, 92410 Ville d'Avray, France*

Abstract

This paper extends sublaminar-based variable kinematics plate finite elements towards the buckling analysis of composite structures. Robust locking-free 4-node and 8-node interpolations are used to build the finite element matrices in terms of fundamental nuclei, invariant with respect to the employed kinematic model of the composite plate. Geometric nonlinearities are accounted for in the von Kármán sense. The classical linearised stability analysis is mainly conducted for sandwich panels, for which different kinematic assumptions are employed for the skins and the core. Global buckling of the sandwich panel as well as short-wavelength wrinkling of the skins are investigated by referring to a variety of case studies, including homogeneous and laminated skins as well as isotropic and orthotropic cores. Convergence studies are performed to establish the minimum number of elements for the local instabilities to be grasped. The proposed computational framework requires a simple 2D mesh and is capable of providing quasi-3D response patterns. This is as demonstrated by numerous case studies that address the transition from global to local buckling, the onset of wrinkling in flat sandwich panels with anisotropic skins under various loading conditions as well as the local face sheet instability occurring in sandwich panels working in bending. It is concluded that the proposed FEM-based tool is computationally efficient and can be advantageously employed in pre-sizing design phases without resorting to full 3D models.

Keywords: Variable kinematics plate model, unified formulation, finite element method, sandwich plate, linear buckling analysis, global/local instabilities, face sheet wrinkling,

¹Corresponding author. Dr.-Ing. Girolamo Di Cara, Email: dicarag@parisnanterre.fr

1. Introduction

Sandwich structures are widely employed in weight-sensitive applications due to their outstanding specific bending stiffness obtained by separating two stiff skins through a thick though lightweight core [1]. By virtue of their high bending rigidity, sandwich panels show thus an improved resistance to buckling [2, 3]. However, it is important to account for the transverse shear deformation occurring in the mechanically weak core because it reduces the critical loads related to the simple bending stiffness [4]. Furthermore, the thin skins are prone to local instabilities referred to as wrinkling, in which the face sheets buckle in a short-wavelength of the order of the core thickness [5]. An outstanding contribution to the understanding of the wrinkling phenomenon has been given by Fagerberg [6–9], ranging from the effects of anisotropy in the face sheets up to the transition from wrinkling to the pure compression failure. It is worth emphasising that this instability does not only arise in compressed struts, but it is likely to occur also in the skin under compression under a global bending deformation [10].

This failure mechanism is often catastrophic because it comes along an important stiffness loss due to the weak mechanical properties of the core and the onset of delamination between the core and the buckled face sheet. Therefore, it is important to accurately calculate the critical wrinkling loads for a reliable sizing of sandwich panels.

The short-wavelength of the wrinkling has called for a representation of this mechanism as a material failure: given the geometric and constitutive properties of skins and core, analytical formulas for the critical loads have been proposed irrespective of the actual loading and boundary conditions of the panel. This approach proves effective inasmuch as it can be employed within large scale models of built-up structures, such as the Global FE Model of an aircraft [11]. An extensive literature review over the analytical wrinkling formulae can be found in [12] and in the more recent critical assessment by Ginot *et al.* [13]. It turns out that the validity of such analytical expressions is confined to specific classes of problems and that they prove rather inaccurate when applied on configurations that do not meet the assumptions upon which they are based.

Three-dimensional (3D) FE models have been developed for investigating the wrinkling failure [14–16], which are, however, too computationally intensive to be used in a preliminary design phase. So-called “unified” approaches based on high-order structural models have been also proposed that are capable of predicting both global buckling and local wrinkling [17–20]. These approaches are attractive because they open the possibility of investigating the interaction between global and local

instabilities [21, 22].

By introducing his “Unified Formulation”, Carrera paved the way for the development of computational tools based on a so-called variable kinematics approach, in which high-order structural models can be tailored depending on the considered problem and the desired accuracy [23]. Dedicated to composite structures, Equivalent Single Layer (ESL) as well as Layer-Wise (LW) models of variable order can be all used by simply selecting an appropriate input. The Sublaminated Generalized Unified Formulation (SGUF) is a formal development of the original Carrera Unified Formulation (CUF) and of Demasi’s Generalized Unified Formulation (GUF) [24] allowing to meet the specific requirements for efficient models of sandwich panels, for which different models are conveniently used to model the thin face sheets and the thick core [25].

CUF models accounting for geometrical nonlinearities, have been developed by Pagani and Carrera for buckling and post-buckling analyses of laminated composite beams and isotropic plates [26–28]. CUF-based beam models have been developed by Hui *et al.* towards post-buckling analyses of sandwich beams accounting for the occurrence of coupled global-local instability [29]. CUF and SGUF models have been also applied successfully to sandwich buckling and wrinkling problems by referring to Navier-type [30] and to Ritz solutions [31]. The Ritz method does in particular allow to broaden the studies towards anisotropic panels with arbitrary boundary conditions. By resorting to high-order in-plane functions, it has been shown that very refined SGUF models are capable of grasping the short wavelength response even in configurations involving anisotropic face sheets and multi-axial loads. These findings are the encouraging starting points for the developments proposed in this paper, in which the Finite Element (FE) implementation of SGUF presented in [32] is extended towards the linearized buckling analysis.

The paper is organized as follows: Sec. 2 briefly recalls the modelling of multilayered panels by variable kinematics plate theories within the framework of Finite Element Method (FEM) and Sec. 3 presents its extension towards geometrical nonlinearities for the linearized stability analysis; in Sec. 4 the numerical tool is assessed by investigating a number of case studies: symmetric cross-ply laminates and sandwich panels with homogeneous as well as anisotropic composite skins under uniaxial compression loads, the onset of local instabilities in the face sheets of sandwich structures which work in bending and the transition from global to local instabilities in symmetric sandwich panels under combined shear and compression loads. Finally, Sec. 5 summarizes the main outcomes and proposes potential future developments.

2. Problem statement

2.1. Geometry description

Let us consider a composite plate occupying the volume $V = \Omega \times [-H/2 \leq z \leq H/2]$, where H represents the total thickness, and $\Omega = [0, a] \times [0, b]$ denotes the reference surface on the (x, y) -plane. The composite plate consists of $p = 1, 2 \dots N_p$ homogeneous and perfectly bonded plies stacked along the thickness direction z , with each ply having a thickness of h_p , as illustrated in Fig. 1. The composite cross-section is further idealized into $k = 1, 2 \dots N_l$ numerical

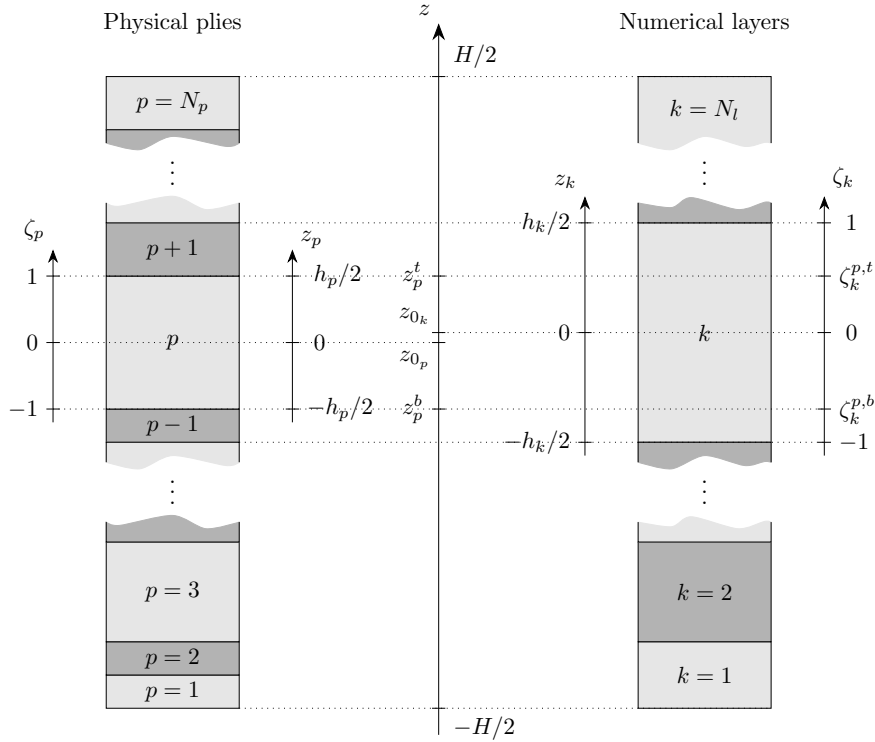


Figure 1: Global z , layer-specific z_k and ply-specific z_p coordinates and non-dimensional layer- and ply-specific coordinates ζ_k and ζ_p within the SGUF formalism.

layers (also named sublaminates) within the SGUF formalism. Each sublaminate has a uniform thickness h_k and it is composed of N_p^k adjacent plies. Local coordinates $z_p \in [-h_p/2, h_p/2]$ and $z_k \in [-h_k/2, h_k/2]$ are introduced along with their corresponding non-dimensional counterparts $\zeta_k \in [-1, 1]$ and $\zeta_p \in [-1, 1]$, in order to define the interpolations across the thickness of the k^{th} sublaminate and the p^{th} ply, respectively:

$$\zeta_{\square} = \frac{2}{h_{\square}} z - \frac{z_t^{\square} + z_b^{\square}}{z_t^{\square} - z_b^{\square}} \quad \text{with } \square = p, k \quad (1)$$

The following relation between the non-dimensional ply-specific and layer-specific coordinates holds:

$$\zeta_p = \frac{h_k}{h_p} \zeta_k + \frac{2}{h_p} (z_{0_k} - z_{0_p}) \quad (2)$$

where z_{0_\square} denotes the mid-plane coordinates of the k^{th} sublaminates ($\square = k$) and the p^{th} ply ($\square = p$), respectively.

2.2. Variable kinematics modelling in SGUF

Within the SGUF approach, the behavior along the thickness direction (z - direction) of the generic variable $\mathcal{U}^k \in \{u_x^k, u_y^k, u_z^k\}$ in the k^{th} sublaminates is defined using a polynomial expansion of order $N_{\mathcal{U}}^k$ as follows

$$\mathcal{U}^k(x, y, z_k) = \sum_{\tau_{\mathcal{U}}=0}^{N_{\mathcal{U}}^k} F_{\tau_{\mathcal{U}}}(\zeta) \hat{\mathcal{U}}_{\tau_{\mathcal{U}}}^k(x, y) \quad (3)$$

The thickness functions $F_{\tau_{\mathcal{U}}}$ are defined by Legendre polynomials and are evaluated in terms of non-dimensional sublaminates specific coordinate ζ_k if the generic variable \mathcal{U}^k is described in ESL sense, otherwise they must be expressed in terms of non-dimensional ply specific coordinate ζ_p if a LW description is employed. It is emphasised that the SGUF notation Eq. (3) implies that arbitrary expansion orders can be used independently for the three displacement components and in different layers. More details about the definition and properties of the thickness functions as well as about the assembly procedures for both ESL and LW descriptions can be found in [25, 32].

2.2.1. Models acronyms

The SGUF approach allows to adopt different kinematic models for individual sublaminates, the overall model is thus denoted by specifying individual sublaminates models. For each sublaminates, the adopted model is uniquely identified by an acronym that is constituted of the letter ‘‘D’’ that states the displacement-based framework, followed by 3 subscripts that identify the approximation used for each of the 3 displacement variables u_i : the letter ‘‘L’’ or ‘‘E’’ is used for LW or ESL descriptions, respectively, and is complemented by the polynomial order N_{u_i} . For example, the acronym D_{L3L1E0} signifies that the sublaminates adopts an LW description with cubic and linear polynomials for the in-plane displacement variables u_x and u_y , respectively, while the out-of-plane displacement u_z remains constant throughout the whole stack of the sublaminates.

Simplified acronyms can be employed when the same expansion order or multilayer description is used for more than one displacement variable. It is frequently the case that the in-plane displace-

ments $u_\alpha (\alpha = 1, 2)$ are modeled in the same way, in which case one subscript can be dropped out without loss of clarity. For instance, if a linear ESL approximation is used for the in-plane variables u_1, u_2 and a quadratic LW approximation is employed for transverse displacement u_3 , the acronym is simplified to D_{E1L2} . Additionally, if all displacement variables are approximated in the same manner, the classical CUF models are obtained and its corresponding notation is used, e.g., ED2 for an ESL description with quadratic polynomials or LD4 for a fourth-order LW approximation.

2.3. FE approximate solution

Within FEM, the unknown functions $\hat{\mathcal{U}}_{\tau_{\alpha i}}^k$ of Eq. (3) are expressed as a linear combination of basis functions that span the space in which the solution is sought in terms of interpolation of nodal unknowns:

$$\hat{\mathcal{U}}_{\tau_{\alpha i}}^k(x, y) = \sum_{i=1}^n N_i(\xi, \eta) \mathcal{U}_{\tau_{\alpha i}}^k \quad (4)$$

where n is the number of FE nodes and N_i are the shape functions over the 2D elementary domain. Four-node Lagrange and eight-node Serendipity quadrilateral elements are used to discretize the reference surface Ω and approximate the solution (see Fig. 2 and Fig. 3).

The C_0^Ω isoparametric interpolation is employed for all the variables of the formulation except for the z -constant term of the transverse shear strains $\gamma_{\mu 3}$. Knowing this term to be responsible of the so-called shear locking pathology for thin plates, the field-compatible approximations QC4 (4-node) and CL8 (8-node) have been used to interpolate it over the element [33, 34]. It is worthwhile noticing that the QC4 interpolation is equivalent to MITC4 proposed by Dvorkin and Bathe in [35] and applied to CUF-based FEs by Cinefra *et al.* [36].

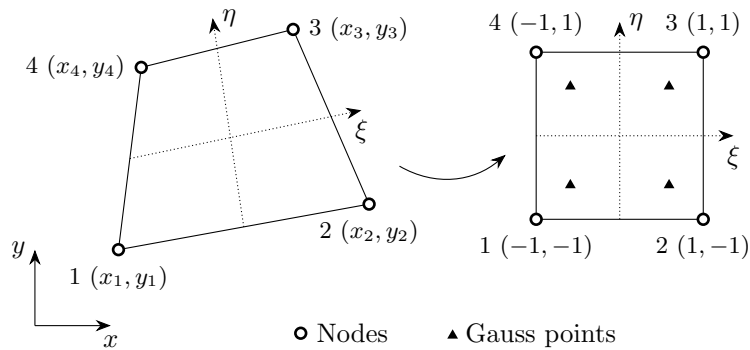


Figure 2: Four-node quadrilateral in the physical Cartesian frame (x, y) and in the natural frame (ξ, η) .

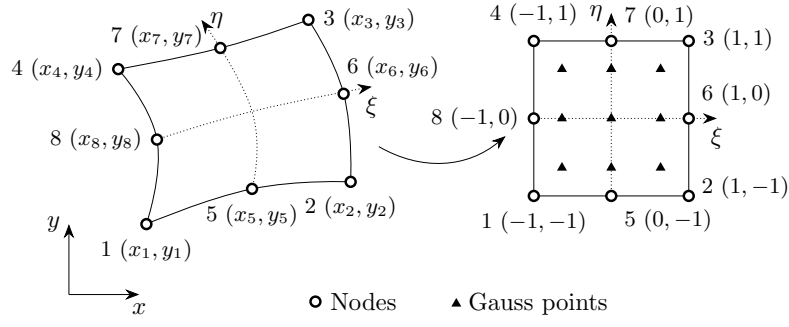


Figure 3: Eight-node quadrilateral in the physical Cartesian frame (x, y) and in the natural frame (ξ, η) .

3. Governing equations for the linearized stability analysis

3.1. Variational statement for bifurcation problems

Within the classical Euler's method, the geometrical nonlinearity is introduced to provide the possibility of a system to have multiple equilibrium solutions under a given load, i.e., to characterise a "bifurcation point". In this framework, the "small perturbation" represents the possible equilibrium configuration adjacent to the "initial" one under the same external actions. Therefore, the incremental form of the Principle of Virtual Work written within the Total Lagrangean approach is linearized as [37]:

$$\int_{V^0} \delta \eta'_{ij} \sigma_{ij(I)} + \delta e'_{ij} C_{ijkl} e'_{kl} dV = 0 \quad (5)$$

Einstein notation is here employed which implies summation over the repeated Latin indices that range in the set $\{1, 2, 3\}$ related to the 3D space as $x_1 \equiv x, x_2 \equiv y, x_3 \equiv z$. The subscript (I) denotes the initial (equilibrium) state characterised by a stress state of finite magnitude, while the superscript $'$ refers to the perturbed configuration. The strains e'_{ij} and η'_{ij} are the contributions to the Green-Lagrange strains E'_{ij} that are linear and quadratic in the perturbation displacements u'_i , respectively:

$$E'_{ij} = e'_{ij}(u'_i) + \eta'_{ij}(u'^2_i) \quad (6)$$

The following additional simplifying assumptions are conveniently introduced to focus on the bifurcation buckling of panels under initial in-plane stresses.

- von Kármán approximation: since the principal buckling mode of in-plane stressed panels concerns the out-of-plane deflection, it is convenient to retain only the nonlinear contribution of the transverse displacement u_3 to the in-plane strains $E'_{\alpha\beta}$. Greek indices are taken in the set

{1, 2} to identify quantities related to the in-plane directions (x, y). Therefore, the perturbation strains reduce to

$$E'_{\alpha\beta} = e'_{\alpha\beta}(u'_i) + \eta'_{\alpha\beta}(u'_3{}^2); \quad E'_{i3} = \epsilon'_{i3} = \frac{1}{2}(u'_{i,3} + u'_{3,i}) \quad (7a)$$

where

$$e'_{\alpha\beta} = \frac{1}{2}(u'_{\alpha,\beta} + u'_{\beta,\alpha}) + u_{3,\alpha}u'_{3,\beta} = \epsilon'_{\alpha\beta} + u_{3,\alpha}u'_{3,\beta}; \quad \eta'_{\alpha\beta} = \frac{1}{2}u'_{3,\alpha}u'_{3,\beta} \quad (7b)$$

and $\epsilon_{ij} = (u_{i,j} + u_{j,i})/2$ is the classical linear strain measure.

- Undeformed pre-stressed configuration: the approximation is next introduced that neglects the changes of geometrical configuration that may be induced by the initial stress state, i.e., $\Omega_t \approx \Omega_0$ with, in particular, $u_3 \approx 0$ in Eq. (7). Therefore the nonlinear perturbation strains are further reduced to

$$E'_{\alpha\beta} = \frac{1}{2}(u'_{\alpha,\beta} + u'_{\beta,\alpha}) + \frac{1}{2}u'_{3,\alpha}u'_{3,\beta} = \epsilon'_{\alpha\beta} + \eta'_{\alpha\beta} \quad (8)$$

- Nonlinear strains are discarded from the definition of the initial in-plane stresses, which are independent of the perturbation:

$$\sigma_{\alpha\beta(I)} = C_{\alpha\beta kl} E_{kl(I)} \approx C_{\alpha\beta kl} \epsilon_{kl(I)} \quad (9)$$

The initial stress is as usual defined as a reference stress state $\sigma_{\alpha\beta(I)}^0$ that is scaled by a load factor λ . The variational formulation eventually yields the following classical linear eigenvalue problem: find λ such that a non-trivial adjacent configuration exists that satisfies

$$\int_{V^0} \delta \eta'_{\alpha\beta} \lambda \sigma_{\alpha\beta(I)}^0 + \delta \epsilon'_{ij} C_{ijkl} \epsilon'_{kl} dV = 0 \quad (10)$$

In this paper, the reference stress state $\sigma_{\alpha\beta(I)}^0 = \sigma_{P(I)}$ is defined by referring to a plane stress setting as

$$\sigma_{P(I)} = \tilde{Q}_{PQ} \epsilon_{Q(I)} \quad (11)$$

where $P, Q \in \{1, 2, 6\}$ are the indices of the compact Voigt notation identifying the in-plane stress and strain components, and $\tilde{Q}_{PQ} = C_{PQ} - C_{P3}C_{3Q}/C_{33}$ are the reduced stiffnesses of the constitutive law accounting for the condition $\sigma_{33} = 0$. The initial strain field $\epsilon_{Q(I)}$ is given either directly as an input (uniform strain), or defined from a previous FE computation. It is worth recalling that the

perturbation is computed for the undeformed geometry, i.e., the strain field is used only to define the initial stress and not for updating the geometry under the initial load. This approximation may come along a certain inaccuracy in particular if the out-of-plane deflection is not small at the onset of the bifurcation.

3.2. Definition of the initial stress matrix

Introducing the plate model assumptions Eq. (3) and the FE discretization Eq. (4) into the variational formulation Eq. (10), and carrying out all integrations and the assembly steps, the discrete form of the eigenvalue problem is obtained:

$$\{\delta \mathbf{U}'\}^T [\mathbf{K} + \lambda \mathbf{K}_\sigma] \{\mathbf{U}'\} = \{\mathbf{0}\} \quad (12)$$

The linear stiffness matrix \mathbf{K} has been already presented in [32], further details will be here omitted for the sake of brevity. The “initial stress” or “geometric stiffness” matrix \mathbf{K}_σ is expressed from Eq. (10) as

$$\{\delta \mathbf{U}'\}^T [\mathbf{K}_\sigma] \{\mathbf{U}'\} = \int_{V^0} \delta \eta'_{\alpha\beta} \sigma_{\alpha\beta(I)}^0 dV = \int_{V^0} \delta \eta'_P \tilde{Q}_{PQ} \epsilon_{Q(I)} dV \quad (13)$$

Substituting the definition of the initial membrane stress

$$\begin{aligned} \int_{V^0} \delta \eta'_P \tilde{Q}_{PQ} \epsilon_{Q(I)} dV = & \int_{V^0} \delta \eta'_1 (\tilde{Q}_{11} \epsilon_{1(I)} + \tilde{Q}_{12} \epsilon_{2(I)} + \tilde{Q}_{16} \epsilon_{6(I)}) + \\ & + \delta \eta'_2 (\tilde{Q}_{12} \epsilon_{1(I)} + \tilde{Q}_{22} \epsilon_{2(I)} + \tilde{Q}_{26} \epsilon_{6(I)}) + \\ & + \delta \eta'_6 (\tilde{Q}_{16} \epsilon_{1(I)} + \tilde{Q}_{26} \epsilon_{2(I)} + \tilde{Q}_{66} \epsilon_{6(I)}) dV \end{aligned} \quad (14)$$

The virtual variations of the incremental strain that is quadratic in the perturbation displacements U' read

$$\delta \eta'_1 = \delta u'_{3,1} u'_{3,1}; \quad \delta \eta'_2 = \delta u'_{3,2} u'_{3,2}; \quad \delta \eta'_6 = \delta u'_{3,1} u'_{3,2} + \delta u'_{3,2} u'_{3,1} \quad (15)$$

The linear strain field of the initial pre-buckling configuration (I) is

$$\epsilon_{1(I)} = u_{1(I),1}; \quad \epsilon_{2(I)} = u_{2(I),2}; \quad \epsilon_{6(I)} = u_{1(I),2} + u_{2(I),1} \quad (16)$$

Thus, dropping out the subscript (I) from the pre-buckling strains

$$\begin{aligned}
\{\delta \mathbf{U}'\}^T [\mathbf{K}_\sigma] \{\mathbf{U}\} &= \int_{V^0} \delta u'_{3,1} (\tilde{Q}_{11}\epsilon_1 + \tilde{Q}_{12}\epsilon_2 + \tilde{Q}_{16}\epsilon_6) u'_{3,1} + \\
&\quad + \delta u'_{3,2} (\tilde{Q}_{12}\epsilon_1 + \tilde{Q}_{22}\epsilon_2 + \tilde{Q}_{26}\epsilon_6) u'_{3,2} + \\
&\quad + \delta u'_{3,1} (\tilde{Q}_{16}\epsilon_1 + \tilde{Q}_{26}\epsilon_2 + \tilde{Q}_{66}\epsilon_6) u'_{3,2} + \\
&\quad + \delta u'_{3,2} (\tilde{Q}_{16}\epsilon_1 + \tilde{Q}_{26}\epsilon_2 + \tilde{Q}_{66}\epsilon_6) u'_{3,1} dV = \\
&= \int_{V^0} \delta u'_{3,1} \left\{ \tilde{Q}_{11}u_{1,1} + \tilde{Q}_{12}u_{2,2} + \tilde{Q}_{16}u_{1,2} + \tilde{Q}_{16}u_{2,1} \right\} u'_{3,1} + \\
&\quad + \delta u'_{3,2} \left\{ \tilde{Q}_{12}u_{1,1} + \tilde{Q}_{22}u_{2,2} + \tilde{Q}_{26}u_{1,2} + \tilde{Q}_{26}u_{2,1} \right\} u'_{3,2} + \\
&\quad + \delta u'_{3,1} \left\{ \tilde{Q}_{16}u_{1,1} + \tilde{Q}_{26}u_{2,2} + \tilde{Q}_{66}u_{1,2} + \tilde{Q}_{66}u_{2,1} \right\} u'_{3,2} + \\
&\quad + \delta u'_{3,2} \left\{ \tilde{Q}_{16}u_{1,1} + \tilde{Q}_{26}u_{2,2} + \tilde{Q}_{66}u_{1,2} + \tilde{Q}_{66}u_{2,1} \right\} u'_{3,1} dV
\end{aligned} \tag{17}$$

Note that only the initial *in-plane* displacements $u_{\alpha(I)}$ are required to define the initial stress matrix. The plate approximation given in Eq. (3) is used for the virtual displacement increments δu_r and the corresponding unknowns u_s ($r, s \in \{1, 2, 3\}$). The summation indexes for the through-thickness expansion of the virtual variation and of the unknown will be μ_{u_r} and τ_{u_s} , respectively. Analogous expressions are hence introduced for the displacements at the initial configuration (I), for which the summation index γ_{u_α} is used:

$$u_{x(I)}^k(x, y, z) = \sum_{\gamma_{u_x}=0}^{N_{u_x}^k} F_{\gamma_{u_x}}(z) \hat{u}_{\gamma_{u_x}}^k(x, y); \quad u_{y(I)}^k(x, y, z) = \sum_{\gamma_{u_y}=0}^{N_{u_y}^k} F_{\gamma_{u_y}}(z) \hat{u}_{\gamma_{u_y}}^k(x, y) \tag{18}$$

where the subscript (I) has been dropped out from the in-plane functions \hat{u}_γ without loss of clarity.

These expressions are substituted into Eq. (17), and the integration over the thickness coordinate z is carried out explicitly (note that only in-plane derivatives occur in the initial stress matrix).

Following the notation proposed in [32], the through-thickness integrals involved in \mathbf{K}_σ are of the form

$$Z_{u_r u_s u_\alpha}^{\mu_{u_r} \tau_{u_s} \gamma_{u_\alpha}} = \int_{z_p^{bot}}^{z_p^{top}} F_{\mu_{u_r}} F_{\tau_{u_s}} F_{\gamma_{u_\alpha}} dz \tag{19}$$

The integration is intended to be carried out over the thickness $h_p = [z_p^{bot}, z_p^{top}]$ of each ply separately since the stresses will depend on the ply-specific stiffness coefficients \tilde{Q}_{PQ}^p .

The initial stress matrix thus reads

$$\begin{aligned}
\{\delta \hat{u}'_\mu\}^T [K_{\mu\tau}^\sigma] \{\hat{u}'_\tau\} = & \int_{\Omega^0} \frac{\partial \delta \hat{u}'_{z\mu z}}{\partial y} \left\{ \right. \\
& \left[\tilde{Q}_{12} Z_{u_z u_z u_x}^{\mu u_z \tau u_z \gamma u_x} \frac{\partial \hat{u}'_{x\gamma u_x}}{\partial x} + \tilde{Q}_{22} Z_{u_z u_z u_y}^{\mu u_z \tau u_z \gamma u_y} \frac{\partial \hat{u}'_{y\gamma u_y}}{\partial y} + \right. \\
& \left. + \tilde{Q}_{26} Z_{u_z u_z u_x}^{\mu u_z \tau u_z \gamma u_x} \frac{\partial \hat{u}'_{x\gamma u_x}}{\partial y} + \tilde{Q}_{26} Z_{u_z u_z u_y}^{\mu u_z \tau u_z \gamma u_y} \frac{\partial \hat{u}'_{y\gamma u_y}}{\partial x} \right] \frac{\partial \hat{u}'_{z\tau u_z}}{\partial y} + \\
& \left[\tilde{Q}_{16} Z_{u_z u_z u_x}^{\mu u_z \tau u_z \gamma u_x} \frac{\partial \hat{u}'_{x\gamma u_x}}{\partial x} + \tilde{Q}_{26} Z_{u_z u_z u_y}^{\mu u_z \tau u_z \gamma u_y} \frac{\partial \hat{u}'_{y\gamma u_y}}{\partial y} + \right. \\
& \left. + \tilde{Q}_{66} Z_{u_z u_z u_x}^{\mu u_z \tau u_z \gamma u_x} \frac{\partial \hat{u}'_{x\gamma u_x}}{\partial y} + \tilde{Q}_{66} Z_{u_z u_z u_y}^{\mu u_z \tau u_z \gamma u_y} \frac{\partial \hat{u}'_{y\gamma u_y}}{\partial x} \right] \frac{\partial \hat{u}'_{z\tau u_z}}{\partial x} \left. \right\} + \\
& + \frac{\partial \delta \hat{u}'_{z\mu z}}{\partial x} \left\{ \right. \\
& \left[\tilde{Q}_{16} Z_{u_z u_z u_x}^{\mu u_z \tau u_z \gamma u_x} \frac{\partial \hat{u}'_{x\gamma u_x}}{\partial x} + \tilde{Q}_{26} Z_{u_z u_z u_y}^{\mu u_z \tau u_z \gamma u_y} \frac{\partial \hat{u}'_{y\gamma u_y}}{\partial y} + \right. \\
& \left. + \tilde{Q}_{66} Z_{u_z u_z u_x}^{\mu u_z \tau u_z \gamma u_x} \frac{\partial \hat{u}'_{x\gamma u_x}}{\partial y} + \tilde{Q}_{66} Z_{u_z u_z u_y}^{\mu u_z \tau u_z \gamma u_y} \frac{\partial \hat{u}'_{y\gamma u_y}}{\partial x} \right] \frac{\partial \hat{u}'_{z\tau u_z}}{\partial y} + \\
& \left[\tilde{Q}_{11} Z_{u_z u_z u_x}^{\mu u_z \tau u_z \gamma u_x} \frac{\partial \hat{u}'_{x\gamma u_x}}{\partial x} + \tilde{Q}_{12} Z_{u_z u_z u_y}^{\mu u_z \tau u_z \gamma u_y} \frac{\partial \hat{u}'_{y\gamma u_y}}{\partial y} + \right. \\
& \left. + \tilde{Q}_{16} Z_{u_z u_z u_x}^{\mu u_z \tau u_z \gamma u_x} \frac{\partial \hat{u}'_{x\gamma u_x}}{\partial y} + \tilde{Q}_{16} Z_{u_z u_z u_y}^{\mu u_z \tau u_z \gamma u_y} \frac{\partial \hat{u}'_{y\gamma u_y}}{\partial x} \right] \frac{\partial \hat{u}'_{z\tau u_z}}{\partial x} \left. \right\} dx dy
\end{aligned} \tag{20}$$

The FE interpolation Eq. (4) is next introduced for the virtual increments $\delta u'_r$, the unknowns u'_s and the initial displacements $u_{\alpha(l)}$, with the summation indices i, j and l , respectively. Since no transverse shear appears in the initial stress matrix, the classical isoparametric interpolation is used for the FE approximation of \mathbf{K}_σ . Differentiation and integration with respect to the in-plane coordinates x, y as they occur in Eq. (20) are carried out according to following notation:

$$\mathcal{I}_{u_r u_s u_\alpha}^{defghn} = \int_{\Omega} \frac{\partial^{d+e} N_{u_r i}}{\partial x^d \partial y^e} \left(\frac{\partial^{h+n} N_{u_\alpha l}}{\partial x^h \partial y^n} \right) \frac{\partial^{f+g} N_{u_s j}}{\partial x^f \partial y^g} dx dy \quad (d, e, f, g, h, n = 0, 1) \tag{21}$$

The *fundamental nuclei* of the geometric stiffness matrix have finally the following expression:

$$\begin{aligned}
\{\delta U'_{\mu i}\}^T [K_{\mu\tau ij}^\sigma] \{U'_{\tau j}\} = \delta U'_{z\mu z i} \left[\right. \\
& \tilde{Q}_{11} Z_{u_z u_z u_x}^{\mu u_z \tau u_z \gamma u_x} \mathcal{I}_{u_z u_z u_x i j l}^{101010} U_{x\gamma u_x l} + \tilde{Q}_{12} Z_{u_z u_z u_y}^{\mu u_z \tau u_z \gamma u_y} \mathcal{I}_{u_z u_z u_y i j l}^{101001} U_{y\gamma u_y l} + \\
& + \tilde{Q}_{16} Z_{u_z u_z u_x}^{\mu u_z \tau u_z \gamma u_x} \mathcal{I}_{u_z u_z u_x i j l}^{101001} U_{x\gamma u_x l} + \tilde{Q}_{16} Z_{u_z u_z u_y}^{\mu u_z \tau u_z \gamma u_y} \mathcal{I}_{u_z u_z u_y i j l}^{101010} U_{y\gamma u_y l} + \\
& + \tilde{Q}_{12} Z_{u_z u_z u_x}^{\mu u_z \tau u_z \gamma u_x} \mathcal{I}_{u_z u_z u_x i j l}^{010110} U_{x\gamma u_x l} + \tilde{Q}_{22} Z_{u_z u_z u_y}^{\mu u_z \tau u_z \gamma u_y} \mathcal{I}_{u_z u_z u_y i j l}^{010101} U_{y\gamma u_y l} + \\
& + \tilde{Q}_{26} Z_{u_z u_z u_x}^{\mu u_z \tau u_z \gamma u_x} \mathcal{I}_{u_z u_z u_x i j l}^{010101} U_{x\gamma u_x l} + \tilde{Q}_{26} Z_{u_z u_z u_y}^{\mu u_z \tau u_z \gamma u_y} \mathcal{I}_{u_z u_z u_y i j l}^{010110} U_{y\gamma u_y l} + \\
& + \tilde{Q}_{16} Z_{u_z u_z u_x}^{\mu u_z \tau u_z \gamma u_x} \mathcal{I}_{u_z u_z u_x i j l}^{011010} U_{x\gamma u_x l} + \tilde{Q}_{26} Z_{u_z u_z u_y}^{\mu u_z \tau u_z \gamma u_y} \mathcal{I}_{u_z u_z u_y i j l}^{011001} U_{y\gamma u_y l} + \\
& + \tilde{Q}_{66} Z_{u_z u_z u_x}^{\mu u_z \tau u_z \gamma u_x} \mathcal{I}_{u_z u_z u_x i j l}^{011001} U_{x\gamma u_x l} + \tilde{Q}_{66} Z_{u_z u_z u_y}^{\mu u_z \tau u_z \gamma u_y} \mathcal{I}_{u_z u_z u_y i j l}^{011010} U_{y\gamma u_y l} + \\
& + \tilde{Q}_{16} Z_{u_z u_z u_x}^{\mu u_z \tau u_z \gamma u_x} \mathcal{I}_{u_z u_z u_x i j l}^{100110} U_{x\gamma u_x l} + \tilde{Q}_{26} Z_{u_z u_z u_y}^{\mu u_z \tau u_z \gamma u_y} \mathcal{I}_{u_z u_z u_y i j l}^{100101} U_{y\gamma u_y l} + \\
& + \tilde{Q}_{66} Z_{u_z u_z u_x}^{\mu u_z \tau u_z \gamma u_x} \mathcal{I}_{u_z u_z u_x i j l}^{100101} U_{x\gamma u_x l} + \tilde{Q}_{66} Z_{u_z u_z u_y}^{\mu u_z \tau u_z \gamma u_y} \mathcal{I}_{u_z u_z u_y i j l}^{100110} U_{y\gamma u_y l} \\
& \left. \right] U'_{z\tau u_z j}
\end{aligned} \tag{22}$$

It is finally noticed that the summation convention over repeated indices implies the sum over the expansion indices γ and l to be carried out for each couple of indices (μ, τ) and (i, j) . As customary in Unified Formulation models, the model-dependent matrix is thus obtained from the *fundamental nuclei* by cycling over all indices and appropriately assembling all ply-specific contributions.

4. Numerical results

The global and local instability phenomena of multilayered structures under different loading conditions are discussed in this section. A first validation of the proposed FE solution is given by addressing the overall buckling of a symmetric cross-ply laminate under a uniaxial compression, for which an exact 3D elasticity solution has been provided by Noor [38]. Global as well as local instabilities (wrinkles) occurring in sandwich panels are subsequently addressed. The effect of geometric and stiffness ratios on the instability pattern is first investigated by referring to a wide sandwich strut subjected to a uniform compressive strain. Present FE results are here compared against the semi-analytical solution obtained by the Navier-type solution [12]. The skew wrinkling occurring in a sandwich plate with anisotropic laminated skins subjected to uniaxial compression is subsequently addressed. Present FEM solutions are compared with respect to analytical results by Fagerberg and Zenkert [8] as well to Ritz-based solutions given by Vescovini *et al* [31]. The one-sided wrinkling

occurring in the compressed skin of a wide sandwich plate in three-point-bending is then considered by referring to a configuration studied by Yuan *et al* [39]. The nonuniform initial stress field is here obtained from a preliminary linear static FE simulation. Results are compared against full 3D FEM simulations obtained with the commercial package Abaqus. A last case study investigates the buckling under combined compression and shear loading, including the transition from global to local instability dependent on the core thickness of a sandwich structure representative of modern aircraft constructions.

4.1. Uniaxial compression of symmetric cross-ply laminates

A preliminary validation of the proposed FE solution is conducted on the overall buckling of uniaxially compressed symmetric laminates. This case study will be labelled Noor-TestCase (No-TC) because it refers to the configuration for which Noor has given a 3D elasticity solution [38]. It consists of a simply-supported square plate composed of a symmetric cross-ply stack $[0^\circ/90^\circ/0^\circ]$ and subjected to a uniform compressive strain along the longitudinal x direction, see Fig. 4. The geometric and elastic properties are given in Tab. 1. Two width-to-thickness ratio are investigated, namely a moderately-thick ($b/H = 10$) plate and a thin ($b/H = 100$) plate. The total thickness of the plies at 0° and 90° is the same: $h_{0^\circ} = H/4$ and $h_{90^\circ} = H/2$.

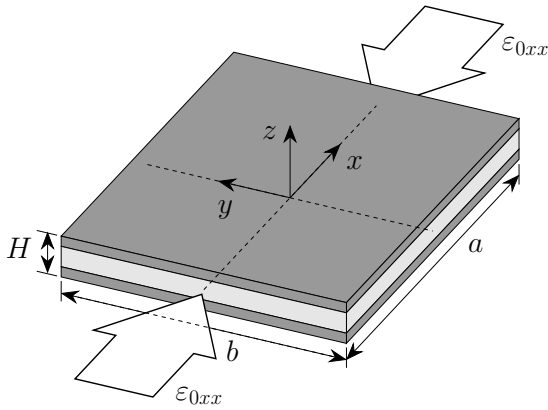


Figure 4: No-TC: Cross-ply laminate geometry.

In order to be consistent with the solution of Ref. [38], the initial stress is purely axial and computed in each ply as

$$\sigma_{0xx}^p = \tilde{C}_{11}^p \epsilon_{0xx} \quad (23)$$

Table 1: No-TC: Geometric and material data.

$a = b = 10$ mm	
$b/H = \{10, 100\} \Rightarrow H = \{1, 0.1\}$ mm	
Material 1	
E_L [MPa]	10
E_T [MPa]	1
ν_{LT}	0.25
ν_{TT}	0.25
G_{LT} [MPa]	0.6
G_{TT} [MPa]	0.5

where the imposed initial strain ϵ_{0xx} is assumed to be unitary. The non-dimensional buckling load is defined as

$$\bar{N} = N_{cr} \frac{b^2}{E_T H^3} \quad \text{with} \quad N_{cr} = \lambda_{cr} \epsilon_{0xx} \sum_{p=1}^{N_p} (\tilde{C}_{11}^p h_p) \quad (24)$$

4.1.1. Convergence study

This case study has been used in a previous work to assess various plate models, including CUF-based models, in the framework of a quasi-analytical Navier-type solution [40]. In the following, the No-TC is used to examine the convergence of the proposed FE solution towards the Navier solution obtained by the same plate models, i.e., the attention is restricted to the discretization error. To this aim, the isoparametric 8-node FE are used for the moderately-thick plate ($b/H = 10$) and the CL8 FE are employed for the thin plate case ($b/H = 100$). Given the symmetry of the problem and of the intended response, the computational domain is restricted to one quarter of the plate, for which regular meshes with $N = 1, 2, 4, 6, 8, 10$ elements along the edges are considered.

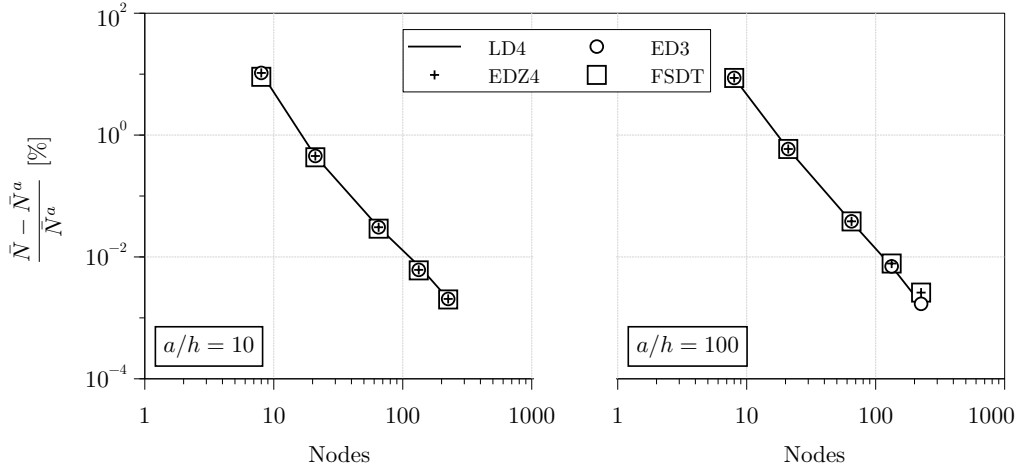


Figure 5: No-TC: Convergence of 8-node FE for selected CUF-models towards the corresponding Navier solution: non-dimensional buckling loads for the quarter plate model.

Fig. 5 reports the convergence curves of the present FE results for several CUF models towards the Navier solution \bar{N}^a obtained by the corresponding models for the orthotropy ratio $E_L/E_T = 10$. The results in Fig. 5 show that the present FE is insensitive to the kinematic model of the plate: more specifically, a quadratic convergence rate is achieved for both the thick and the thin plate and for ESL, Zig-Zag or LW models, irrespective of the polynomial order. Very similar behaviors are obtained for different orthotropy ratios E_L/E_T , whose results are not reported for the sake of conciseness.

Table 2: No-TC: Non-dimensional uniaxial buckling load $\bar{N} = N_{cr}b^2/E_T H^3$ of a three-ply symmetric square plate loaded in compression with an imposed uniform strain: influence of different boundary conditions for a moderately-thick ($b/H = 10$) and thin ($b/H = 100$) plate and varying the orthotropy ratio E_L/E_T . Results obtained with 10×10 8-node elements for the quarter plate.

Model	E_L/E_T								
	3			20			40		
	Boundary conditions			Boundary conditions			Boundary conditions		
	SF	SS	SC	SF	SS	SC	SF	SS	SC
<i>a/h = 10</i>									
LD4	2.1575	5.3052	9.2446	10.9448	15.0197	22.3841	17.6416	22.8812	32.3409
LD3	2.1575	5.3052	9.2447	10.9448	15.0197	22.3845	17.6416	22.8812	32.3417
LD2	2.1577	5.3067	9.2595	10.9464	15.0464	22.6827	17.6460	22.9690	33.0632
LD1	2.1696	5.3583	9.3663	11.0832	15.2144	22.8904	18.0010	23.3474	33.4903
EDZ4	2.1579	5.3054	9.2491	10.9558	15.0468	22.6097	17.6711	22.9740	32.9270
ED4	2.1580	5.3058	9.2505	10.9564	15.0513	22.6664	17.6718	22.9923	33.1022
ED3	2.1582	5.3061	9.2534	10.9592	15.0552	22.6825	17.6782	23.0022	33.1372
ED2	2.1756	5.3557	9.4139	11.4075	15.6459	24.2536	18.8590	24.4817	34.9639
ED1	2.2387	5.6321	9.8844	11.4412	15.8102	24.5099	18.8753	24.5912	37.1383
FSDT ($\kappa = 5/6$)	2.1789	5.3992	9.3751	11.0325	15.3514	23.5703	17.7343	23.4529	35.0266
<i>a/h = 100</i>									
LD4	2.2889	5.7489	10.6568	14.4829	19.6494	31.6866	28.7411	35.9422	56.3383
LD3	2.2889	5.7489	10.6568	14.4829	19.6495	31.6866	28.7411	35.9422	56.3383
LD2	2.2889	5.7489	10.6571	14.4830	19.6498	31.6943	28.7413	35.9436	56.3676
LD1	2.2983	5.7994	10.7663	14.4940	19.6964	31.7946	28.7595	35.9967	56.4735
EDZ4	2.2890	5.7489	10.6573	14.4834	19.6499	31.6934	28.7428	35.9440	56.3639
ED4	2.2891	5.7489	10.6575	14.4838	19.6499	31.6955	28.7428	35.9443	56.3721
ED3	2.2892	5.7489	10.6577	14.4839	19.6499	31.6960	28.7430	35.9443	56.3726
ED2	2.2894	5.7495	10.6600	14.4916	19.6600	31.7266	28.7732	35.9804	56.4775
ED1	2.3622	6.0718	11.2957	14.5657	19.9422	32.2725	28.8487	36.2580	57.0139
FSDT ($\kappa = 5/6$)	2.2892	5.7500	10.6377	14.4854	19.6553	31.6994	28.7463	35.9554	56.4184

4.1.2. Influence of boundary conditions

Based on the accuracy of the present FE solution, a set of new results is next proposed that extend the No-TC towards different boundary conditions. The square plate is considered simply-supported (S) along the edges parallel to the y -axis, whereas the edges parallel to the x -axis may

be simply-supported (S), clamped (C) or free (F). The symmetry of the fundamental buckling mode is again exploited and the computational model reduced to the quarter plate. The fine mesh with 10×10 8-node elements is used.

Tab. 2 reports the non-dimensional buckling load defined in Eq. (24) for the moderately-thick and thin three-ply laminate and for three different values of the orthotropy ratio E_L/E_T . Increasing the orthotropy ratio is shown to affect the modeling error: for the thick plate in SC configuration, the quadratic ESL model ED2 has an error of approximately 2% for $E_L/E_T = 3$ with respect to the most refined model LD4, which increases to approximately 8% if $E_L/E_T = 40$. The modeling error is shown to be affected to a minor extent by the boundary conditions. It is worth noticing that the ED1 model substantially overestimates the critical load, with errors ranging from 3% (thin plate, SF configuration) up to nearly 15% (thick plate, SC configuration): this is due to the Poisson locking pathology originated by the constant transverse normal stretch in conjunction with the conventional 3D constitutive law [41]. The FSDT kinematics ED₁₀ is obviously free from this pathology, and the use of a shear correction factor $\kappa = 5/6$ allows to match the LD4 solution with remarkable accuracy.

4.2. Global and local buckling of sandwich struts

The capability of the present FE to accurately compute both global buckling and local (wrinkling) loads is next demonstrated by referring to the case study proposed by D’Ottavio and Polit [12], which will be labelled D’Ottavio TestCase (DO-TC) hereinafter. A simply-supported sandwich panel subjected to uniaxial compression along the longitudinal x -direction is considered as shown in Fig. 6. The plane strain assumption is exploited to confine the problem to the (xz) -plane; this is accomplished in the present FEM by using only one element along the width and constraining the displacement u_y at all nodes. The boundary conditions applied to the sandwich panel are thus:

$$u_z(x = \pm a/2, y, z) = u_y(x, y, z) = 0 \quad (25)$$

The geometric and material properties are listed in Tab. 3. The sandwich strut has a total thickness $H = 2f + 2c = 50$ mm, a length of $a = 5H$ for promoting the short-wavelength wrinkling instability, and a unit width ($b = 1$ mm). The role of geometric and material properties on the buckling instability of the sandwich is highlighted by introducing the following three characteristic parameters: the *face-to-core thickness ratio* $R_f = f/H$, the *core-to-face stiffness ratio* $k = E_x^c/E_x^f$ and the *core orthotropy ratio* $\chi = E_x^c/E_z^c$. It is noticed that all Poisson’s ratios are set to zero, which ensures a purely axial stress state from the uniformly strained initial condition.

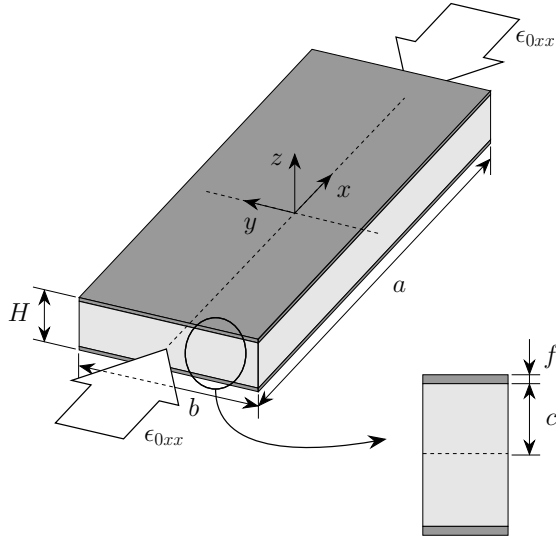


Figure 6: DO-TC: Sandwich beam-plate geometry.

Table 3: DO-TC: Geometric and material data.

$a = 5H; b = 1 \text{ mm}; H = 50 \text{ mm}$		
$f = R_f H; 2c = H - 2f$		
	Core (c)	Facesheet (f)
$\theta [^\circ]$	0	0
$E_x [\text{GPa}]$	χE_z^c	70
$E_y [\text{GPa}]$	χE_z^c	70
$E_z [\text{GPa}]$	$k E_x^f$	70
ν	0	0
$G_{xy} [\text{GPa}]$	$0.5 E_x^c$	35
$G_{xz} [\text{GPa}]$	$0.5 E_z^c$	35
$G_{yz} [\text{GPa}]$	$0.5 E_z^c$	35

4.2.1. Convergence study

A preliminary analysis is carried out to establish the convergence behavior of the proposed 4- and 8-node FE. The in-plane discretization involves $N = 32, 64, 128, 256$ QC4 or $N = 16, 32, 64, 128$ CL8 elements along the x -direction, while only one element is used along the width direction of the panel.

Tab. 4 lists the critical buckling load N_{cr} , defined as in Eq. (24), and the corresponding buckling modes for different combinations of the three parameters R_f, k and χ . In order to establish an “honest” correlation between QC4 and CL8 results, the number of nodes is appended, in subscript, to the number of elements. The high-order LD4 model has been used in the convergence study and the FE convergence is defined with respect to the Navier-type solution obtained with the same kinematic model.

The convergence rate for the buckling loads obtained by the QC4 and CL8 elements is displayed in Fig. 7 and Fig. 8, respectively, for different sandwich configurations defined by the three characteristic ratios R_f, k and χ . The buckled shape obtained with the most refined mesh is also depicted, which shows that the different configurations can trigger overall buckling (one half-wave of length a) or local wrinkling (several half-waves of length $\leq c$). Quadratic and cubic convergence rates are found for the QC4 and CL8 elements, respectively. This high rate is attributed to the plane strain assumption and the absence of mesh refinement along the width. Despite the same convergence

rate is found irrespective of the global or local buckling mode, it is noticed that short-wavelength patterns come along with a generally higher error value.

Figure 7: DO-TC: QC4 convergence for critical buckling load N_{cr} for different sandwich configurations (LD4 model).

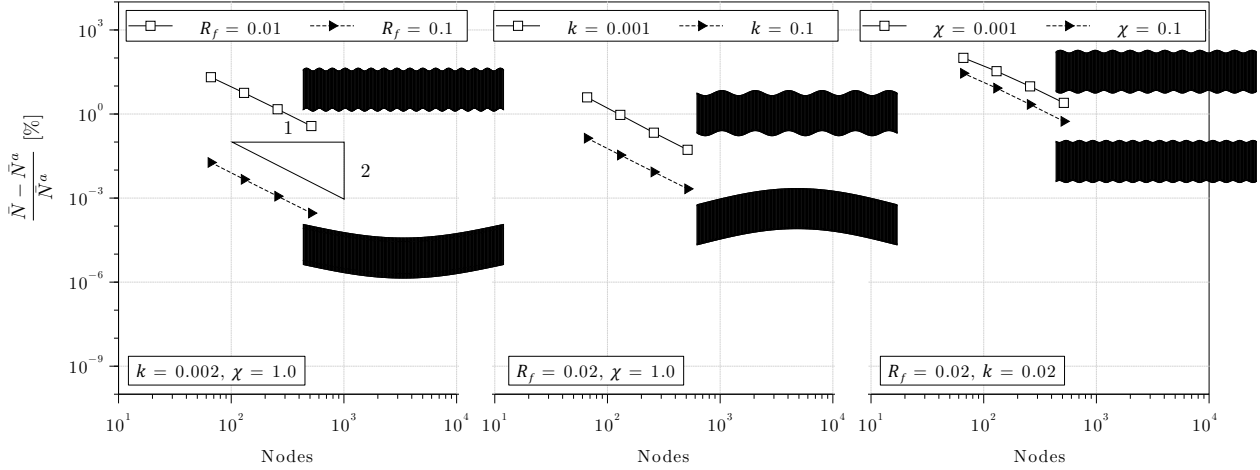
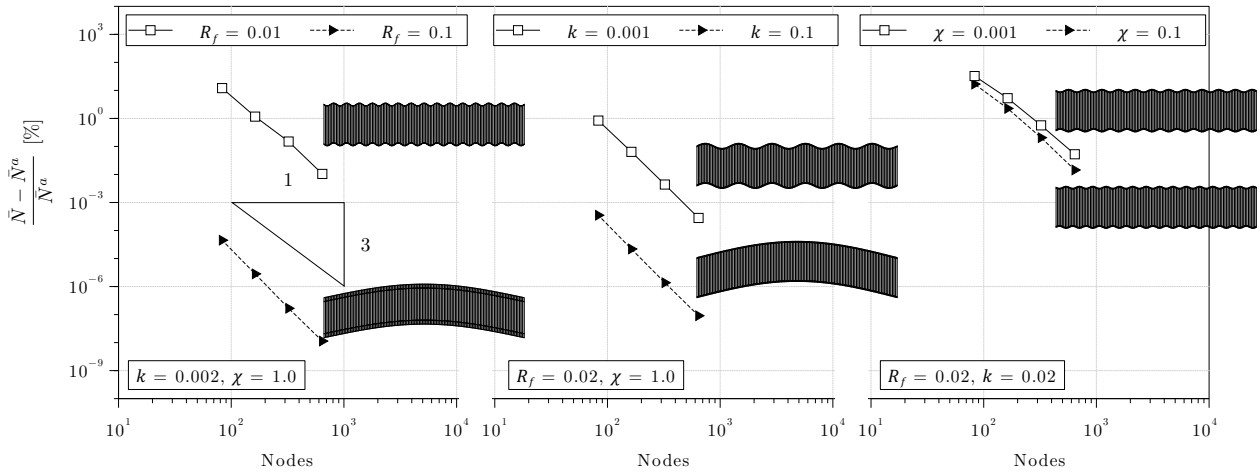


Figure 8: DO-TC: CL8 convergence for critical buckling load N_{cr} for different sandwich configurations (LD4 model).



Further insight about the convergence behavior of the proposed elements is obtained with the numerical data reported in Tab. 4. Here, the buckling mode is identified by specifying in the superscript appended to the buckling load, the number of half-waves along the x -direction and whether the buckled shape is antisymmetric (A) or symmetric (S). Percent differences with respect to the Navier solution are also reported in parentheses. The results show that the discretization error comes along an incorrectly resolved buckling mode. For all the configurations studied in this case study, a percent difference of $< 0.5\%$ in the buckling load is found to provide the correct number of wrinkles of the buckling mode. The results suggest the following additional considerations.

Table 4: DO-TC: Critical buckling loads N_{cr} [N/mm] of LD4 model for different meshes with QC4 and CL8 elements. Number of half-waves and modal shape – antisymmetric (A) or symmetric (S) – are appended in superscript. The values in parentheses indicate the percent differences with respect to Navier solution.

		$R_f (k = 0.002, \chi = 1.0)$			$k (R_f = 0.02, \chi = 1.0)$			$\chi (R_f = 0.02, k = 0.02)$		
		0.01	0.1	0.001	0.1	0.001	0.1	0.001	0.1	0.1
Navier		839.00 ^{31,A}	3528.0 ^{1,A}	948.46 ^{12,A}	19791 ^{1,A}	2758.0 ^{24,S}	6689.1 ^{30,S}			
QC4	256 ₅₁₄	842.12 ^{31,A} (0.37)	3528.0 ^{1,A} (< 0.01)	948.96 ^{12,A} (0.05)	19792 ^{1,A} (< 0.01)	2827.0 ^{23,S} (2.50)	6725.7 ^{30,S} (0.55)			
	128 ₂₅₈	851.42 ^{30,A} (1.48)	3528.1 ^{1,A} (< 0.01)	950.51 ^{12,A} (0.22)	19793 ^{1,A} (0.01)	3025.6 ^{22,S} (9.70)	6836.1 ^{29,S} (2.20)			
	64 ₁₃₀	886.64 ^{26,A} (5.68)	3528.2 ^{1,A} (< 0.01)	957.29 ^{12,A} (0.93)	19798 ^{1,A} (0.03)	3689.9 ^{20,S} (33.8)	7250.9 ^{26,S} (8.40)			
	32 ₆₆	1012.3 ^{19,A} (20.6)	3528.7 ^{1,A} (0.02)	985.76 ^{11,A} (3.93)	19819 ^{1,A} (0.14)	5542.1 ^{16,S} (101)	8587.2 ^{19,S} (28.4)			
CL8	128 ₆₄₂	839.08 ^{31,A} (0.01)	3528.0 ^{1,A} (< 0.01)	948.46 ^{12,A} (< 0.01)	19791 ^{1,A} (< 0.01)	2759.5 ^{24,S} (0.05)	6690.0 ^{30,S} (0.01)			
	64 ₃₂₃	840.25 ^{31,A} (0.15)	3528.0 ^{1,A} (< 0.01)	948.50 ^{12,A} (< 0.01)	19791 ^{1,A} (< 0.01)	2773.6 ^{23,S} (0.57)	6702.9 ^{30,S} (0.21)			
	32 ₁₆₃	848.73 ^{29,A} (1.16)	3528.0 ^{1,A} (< 0.01)	949.07 ^{12,A} (0.06)	19791 ^{1,A} (< 0.01)	2903.7 ^{22,S} (5.28)	6841.2 ^{28,S} (2.27)			
	16 ₈₃	940.39 ^{11,A} (12.1)	3528.0 ^{1,A} (< 0.01)	956.42 ^{12,A} (0.84)	19791 ^{1,A} (< 0.01)	3655.7- (32.5)	7812.0 ^{11,S} (16.8)			

Subscript identifies the number of nodes in the mesh.

Table 5: DO-TC: Uniaxial buckling loads N_{cr} [N/mm] of a sandwich panel loaded in compression with an imposed uniform strain: influence of core model for different sandwich configurations. Bold values identify the converged solution asking for the lowest number of nodal DOFs.

Model (nDOF)	R_f ($k = 0.002, \chi = 1.0$)		k ($R_f = 0.02, \chi = 1.0$)		χ ($R_f = 0.02, k = 0.02$)	
	0.01	0.1	0.001	0.1	0.001	0.1
Ansys [12]	818.80 ^{31,A}	3528.0 ^{1,A}	945.93 ^{13,A}	19792 ^{1,A}	2767.6 ^{23,S}	6464.9 ^{33,A}
Navier (LM4) [12]	813.47 ^{32,A/S}	3528.0 ^{1,A}	945.02 ^{13,A}	19791 ^{1,A}	2758.0 ^{24,S}	6426.9 ^{33,A/S}
LD4 (39)	840.25 ^{31,A}	3528.0 ^{1,A}	948.50 ^{12,A}	19791 ^{1,A}	2773.6 ^{23,S}	6702.9 ^{30,S}
FSDT/ED7 (28)	815.63 ^{31,A}	3528.2 ^{1,A}	945.40 ^{13,A}	19792 ^{1,A}	2776.7 ^{23,S}	6461.2 ^{33,A}
FSDT/ED ₇₆ (27)	815.63 ^{31,A}	3528.2 ^{1,A}	945.40 ^{13,A}	19792 ^{1,A}	2776.8 ^{23,S}	6461.2 ^{33,A}
FSDT/ED ₇₅ (26)	818.19 ^{31,S}	3528.2 ^{1,A}	945.40 ^{13,A}	19792 ^{1,A}	2776.8 ^{23,S}	6468.1 ^{33,S}
FSDT/ED ₇₄ (25)	828.95 ^{30,A}	3528.2 ^{1,A}	945.40 ^{13,A}	19792 ^{1,A}	2777.1 ^{23,S}	6476.2 ^{32,A}
FSDT/ED ₇₃ (24)	875.97 ^{29,S}	3528.2 ^{1,A}	949.37 ^{13,S}	19792 ^{1,A}	2777.1 ^{23,S}	6695.7 ^{30,S}
FSDT/ED ₇₂ (23)	1029.1 ^{26,A}	3528.2 ^{1,A}	960.12 ^{12,A}	19792 ^{1,A}	2807.2 ^{23,S}	7734.6 ^{25,A}
FSDT/ED ₆₇ (26)	816.91 ^{31,S}	3528.2 ^{1,A}	945.51 ^{13,A}	19792 ^{1,A}	2776.7 ^{23,S}	6467.4 ^{33,S}
FSDT/ED6 (25)	818.19 ^{31,S}	3528.2 ^{1,A}	945.51 ^{13,A}	19792 ^{1,A}	2776.8 ^{23,S}	6468.1 ^{33,S}
FSDT/ED ₆₅ (24)	818.19 ^{31,S}	3528.2 ^{1,A}	945.51 ^{13,A}	19792 ^{1,A}	2776.8 ^{23,S}	6468.1 ^{33,S}
FSDT/ED ₆₄ (23)	830.84 ^{31,A}	3528.2 ^{1,A}	945.51 ^{13,A}	19792 ^{1,A}	2777.1 ^{23,S}	6486.6 ^{32,A}
FSDT/ED ₆₃ (22)	875.97 ^{29,S}	3528.2 ^{1,A}	949.37 ^{13,S}	19792 ^{1,A}	2777.1 ^{23,S}	6695.7 ^{30,S}
FSDT/ED ₆₂ (21)	1029.3 ^{26,A}	3528.2 ^{1,A}	960.15 ^{12,A}	19792 ^{1,A}	2807.2 ^{23,S}	7736.9 ^{25,A}
FSDT/ED ₅₇ (24)	819.70 ^{31,A}	3528.2 ^{1,A}	945.51 ^{13,A}	19792 ^{1,A}	2776.7 ^{23,S}	6481.9 ^{32,A}
FSDT/ED ₅₆ (23)	819.70 ^{31,A}	3528.2 ^{1,A}	945.51 ^{13,A}	19792 ^{1,A}	2776.8 ^{23,S}	6481.9 ^{32,A}
FSDT/ED5 (22)	825.58 ^{31,S}	3528.2 ^{1,A}	945.51 ^{13,A}	19792 ^{1,A}	2776.8 ^{23,S}	6486.6 ^{32,A}
FSDT/ED ₅₄ (21)	830.84 ^{31,A}	3528.2 ^{1,A}	945.51 ^{13,A}	19792 ^{1,A}	2777.1 ^{23,S}	6486.6 ^{32,A}
FSDT/ED ₅₃ (20)	877.92 ^{29,S}	3528.2 ^{1,A}	949.88 ^{13,S}	19792 ^{1,A}	2777.1 ^{23,S}	6719.9 ^{30,S}
FSDT/ED ₅₂ (19)	1029.3 ^{26,A}	3528.2 ^{1,A}	960.15 ^{12,A}	19792 ^{1,A}	2807.2 ^{23,S}	7736.9 ^{25,A}
FSDT/ED ₄₇ (22)	822.55 ^{32,S}	3528.2 ^{1,A}	948.67 ^{12,A}	19792 ^{1,A}	2776.7 ^{23,S}	6586.5 ^{32,S}
FSDT/ED ₄₆ (21)	825.11 ^{32,A}	3528.2 ^{1,A}	948.67 ^{12,A}	19792 ^{1,A}	2776.8 ^{23,S}	6595.8 ^{32,S}
FSDT/ED ₄₅ (20)	825.58 ^{31,S}	3528.2 ^{1,A}	948.73 ^{12,A}	19792 ^{1,A}	2776.8 ^{23,S}	6595.8 ^{32,S}
FSDT/ED4 (19)	840.77 ^{31,A}	3528.2 ^{1,A}	948.73 ^{12,A}	19792 ^{1,A}	2777.1 ^{23,S}	6719.9 ^{30,S}
FSDT/ED ₄₃ (18)	877.92 ^{29,S}	3528.2 ^{1,A}	949.88 ^{13,S}	19792 ^{1,A}	2777.1 ^{23,S}	6719.9 ^{30,S}
FSDT/ED ₄₂ (17)	1030.5 ^{26,A}	3528.2 ^{1,A}	961.29 ^{12,A}	19792 ^{1,A}	2807.2 ^{23,S}	7780.7 ^{25,A}
FSDT/ED ₃₇ (20)	824.17 ^{32,S}	3528.2 ^{1,A}	948.67 ^{12,A}	19792 ^{1,A}	2789.0 ^{23,S}	6880.0 ^{31,A}
FSDT/ED ₃₆ (19)	825.11 ^{32,A}	3528.2 ^{1,A}	948.67 ^{12,A}	19792 ^{1,A}	2789.1 ^{23,S}	6880.0 ^{31,A}
FSDT/ED ₃₅ (18)	827.64 ^{32,S}	3528.2 ^{1,A}	948.73 ^{12,A}	19792 ^{1,A}	2789.1 ^{23,S}	6967.5 ^{30,A}
FSDT/ED ₃₄ (17)	840.77 ^{31,A}	3528.2 ^{1,A}	948.73 ^{12,A}	19792 ^{1,A}	2790.9 ^{23,S}	6967.5 ^{30,A}
FSDT/ED3 (16)	888.46 ^{30,S}	3528.2 ^{1,A}	960.60 ^{13,S}	19792 ^{1,A}	2790.9 ^{23,S}	7780.7 ^{25,A}
FSDT/ED ₃₂ (15)	1030.5 ^{26,A}	3528.2 ^{1,A}	961.29 ^{12,A}	19792 ^{1,A}	2807.4 ^{23,S}	7780.7 ^{25,A}
FSDT/ED ₂₇ (18)	824.17 ^{32,S}	3528.3 ^{1,A}	958.51 ^{13,S}	19877 ^{1,A}	2789.0 ^{23,S}	7182.5 ^{35,S}
FSDT/ED ₂₆ (17)	826.32 ^{32,A}	3528.3 ^{1,A}	958.51 ^{13,S}	19877 ^{1,A}	2789.1 ^{23,S}	7188.4 ^{36,A}
FSDT/ED ₂₅ (16)	827.64 ^{32,S}	3528.3 ^{1,A}	958.51 ^{13,S}	19877 ^{1,A}	2789.1 ^{23,S}	7222.9 ^{34,S}
FSDT/ED ₂₄ (15)	841.24 ^{31,A}	3528.3 ^{1,A}	959.94 ^{13,A}	19877 ^{1,A}	2790.9 ^{23,S}	7381.4 ^{34,A}
FSDT/ED ₂₃ (14)	888.46 ^{30,S}	3528.3 ^{1,A}	960.60 ^{13,S}	19877 ^{1,A}	2790.9 ^{23,S}	7810.7 ^{31,S}
FSDT/ED2 (13)	1037.4 ^{27,A}	3528.3 ^{1,A}	980.86 ^{12,A}	19877 ^{1,A}	2807.4 ^{23,S}	9245.2 ^{1,A}
FSDT/ED ₁₇ (16)	826.32 ^{32,A}	3528.3 ^{1,A}	958.82 ^{13,S}	19877 ^{1,A}	6606.7 ^{36,S}	7186.8 ^{34,S}
FSDT/ED ₁₆ (15)	826.32 ^{32,A}	3528.3 ^{1,A}	958.83 ^{13,S}	19877 ^{1,A}	6651.4 ^{35,S}	7188.4 ^{36,A}
FSDT/ED ₁₅ (14)	841.24 ^{31,A}	3528.3 ^{1,A}	958.83 ^{13,S}	19877 ^{1,A}	6651.4 ^{35,S}	7224.6 ^{34,S}
FSDT/ED ₁₄ (13)	841.24 ^{31,A}	3528.3 ^{1,A}	959.94 ^{13,A}	19877 ^{1,A}	6982.1 ^{35,A}	7381.4 ^{34,A}
FSDT/ED ₁₃ (12)	909.37 ^{28,S}	3528.3 ^{1,A}	960.94 ^{13,S}	19877 ^{1,A}	7279.9 ^{33,S}	7830.1 ^{32,S}
FSDT/ED ₁₂ (11)	1037.4 ^{27,A}	3528.3 ^{1,A}	980.86 ^{12,A}	19877 ^{1,A}	9032.1 ^{30,A}	9245.2 ^{1,A}

At least four linear (4-nodes) elements appear to be necessary to properly resolve the half-wave of the wrinkling mode. Nevertheless, percent differences in the buckling load prediction may vary from $\approx 1.5\%$ for the thinnest face sheet configuration, up to $\approx 2\%$ and $\approx 10\%$ for orthotropic cores. If quadratic (8-nodes) elements are used, two elements per half-wave can accurately predict the buckling load (percent differences $< 0.6\%$) and buckled shape.

The following comments can be further made concerning the instability mode triggered depending on the sandwich configuration. It is obvious that overall buckling occurs for either thick faces ($R_f = 0.1$) or a stiff core ($k = 0.1$). In all other cases, the lowest critical load corresponds to a wrinkling-type instability, whose wave-length depends on the characteristic ratios of the sandwich section as well as on the core orthotropy ratio χ . This parameter is further shown to be important for defining whether the mode is antisymmetric or symmetric: it appears that the symmetric mode is triggered when the in-plane stiffness of the core is less than its transverse stiffness, i.e., typically in the case of honeycomb structure. For $\chi = 1$ (isotropic cores) the dominant modal shape is shown to be the antisymmetric one.

4.2.2. Model assessment

The DO-TC is next used to perform a model assessment for investigating the influence of the kinematic model of the core on the computed buckling mode. Based on the previous convergence study, a mesh of 64×1 CL8 elements will be used. The face sheets are modelled according to FSDT, whilst the core model is progressively refined by increasing the order of the theory, ranging from ED_{12} up to $ED_{77} \equiv ED7$. Indeed, FSDT is found to be adequate to represent the buckling phenomenon in the thin face sheets [31]. On the other hand, according to the sandwich configuration, the through-thickness approximation in the core must be enhanced to grasp the correct buckling mode.

The buckling loads and corresponding modes obtained with different kinematic models of the core, are reported for the previously investigated sandwich configurations in Tab. 5. Values in parentheses indicate the number of nodal DOFs of the plate model. Entries in bold emphasize the converged solutions with respect to the core model, obtained with the lowest number of nodal DOFs. Two results presented in [12] are used for comparison:

Solid FEM: A converged FEM solution obtained with the commercial software Ansys and continuum elements. A 2D mesh of 4-nodes elements is used to compute the plane strain problem in

the (xz) -plane: 256 elements are introduced along the longitudinal (x) direction, while 4 and 60 elements are used to discretize along the thickness the face sheets and the core, respectively.

Navier: The mixed CUF model LM4, with an enhanced description of the core obtained by subdividing the core ply into 3 computational layers. This model provides a converged solution with respect to the solid FEM.

Present FE results obtained with the high-order LW model LD4 and the same mesh of the SGUF models are also reported.

Overall buckling occurs for thick face sheets ($k = 0.002$, $R_f = 0.1$, $\chi = 1.0$) and stiff cores ($k = 0.1$, $R_f = 0.02$, $\chi = 1.0$). In this case, the core works essentially in shear and the model ED₃₂ ($N_{u_x} = 3$, $N_{u_z} = 2$) guarantees a converged solution. Very small errors are found if lower-order core kinematics is used, and even an FSDT model (not reported) proves sufficiently accurate. The situation is altogether different when the short wave-length wrinkling occurs, i.e., as the axial rigidity of the sandwich decreases due to thin face sheets or soft cores. In this case, the core provides the elastic support for the buckled face sheets and refined kinematics should be accordingly used for accurately capturing the important core warping and transverse stretch. The SGUF model FSDT/ED₇₆ has proven able to cope with the local response for all the sandwich panel configurations here presented: quasi-3D solution are recovered while drastically reducing the number of DOFs with respect to conventional LW models that adopt the same kinematics for all layers. In this context, it is worth noticing that the FSDT/ED4 model yields in most cases practically the same results as the LD4 model with approximately the half of the nodal DOF (19 against 39 of the LD4 model). Some discrepancies are appreciable only in the last two columns of Tab. 5, i.e., for wrinkling modes characterized by a very short wave-length. In this case, the wave-length is in fact approximately only 10 times larger than the face sheet thickness, a situation for which the classical FSDT model reaches its limit of applicability.

4.3. Skew wrinkling of anisotropic face sheets under uniaxial load

In this section, the potential of the proposed variable kinematics plate elements is challenged against local instabilities developing over the surface of the 2D computational domain. To this aim, we draw upon the study conducted by Fagerberg and Zenkert in Ref. [6], which investigates a sandwich panel with anisotropic face sheets. Henceforth, we shall denote this case study as Fagerberg-TestCase (F-TC). The geometric and material properties are given in Tab. 6. The sandwich panel

is clamped at its lateral edges and subjected to a unitary stress resultant N_{0xx} in the longitudinal direction as illustrated in Fig. 9.

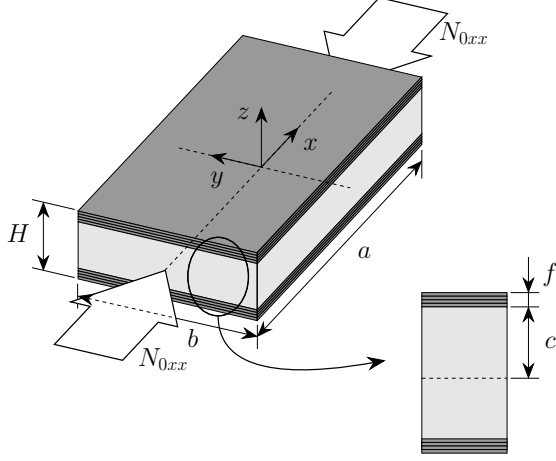


Figure 9: F-TC: Sandwich plate geometry.

Table 6: F-TC: Geometric and material data.

	Core (c)	Facesheet (f)
$a = 200$ mm; $b = 150$ mm		
$f = 1$; $2c = 50$ mm		
$H = 52$ mm		
E_1 [MPa]	107000	20
E_2 [MPa]	15000	20
E_3 [MPa]	15000	20
ν	0.3	0.25
G_{12} [MPa]	4300	13
G_{13} [MPa]	4300	13
G_{23} [MPa]	4300	13

The sandwich panel has a symmetric cross-section and each face sheet consists of a symmetric cross-ply laminate made up of four plies of uniform thickness, see Fig. 10a. The anisotropy is introduced by rotating the principal laminate directions of an angle α with respect to the x, y reference frame of the plate. The anisotropy of the face sheet significantly influences the wrinkle pattern. Wrinkles, which in an isotropic material would typically occur perpendicular to the loading direction, deviate from this orientation due to the anisotropic nature of the face sheet. Instead, they are formed at an angle φ relative to the loading direction. Fig. 10b illustrates the definitions of the angles α and φ .

4.3.1. Pre-buckling

The initial strain field, resulting from the applied uniform stress resultant N_{0xx} , is determined by employing the Classical Lamination Theory (CLT) within the plane stress framework as

$$\epsilon_{0xx} = a_{11} N_{0xx}; \quad \epsilon_{0yy} = a_{12} N_{0xx}; \quad \epsilon_{0xy} = a_{16} N_{0xx} \quad (26)$$

where the coefficients a_{11} , a_{12} and a_{16} are obtained upon inverting the membrane stiffness matrix A .

The pre-buckling stress state is then evaluated for individual plies as:

$$\begin{aligned} \sigma_{0xx}^p &= \tilde{Q}_{11}^p \epsilon_{0xx} + \tilde{Q}_{12}^p \epsilon_{0yy} + \tilde{Q}_{16}^p \gamma_{0xy} \\ \sigma_{0yy}^p &= \tilde{Q}_{12}^p \epsilon_{0xx} + \tilde{Q}_{22}^p \epsilon_{0yy} + \tilde{Q}_{26}^p \gamma_{0xy} \\ \sigma_{0xy}^p &= \tilde{Q}_{16}^p \epsilon_{0xx} + \tilde{Q}_{26}^p \epsilon_{0yy} + \tilde{Q}_{66}^p \gamma_{0xy} \end{aligned} \quad (27)$$

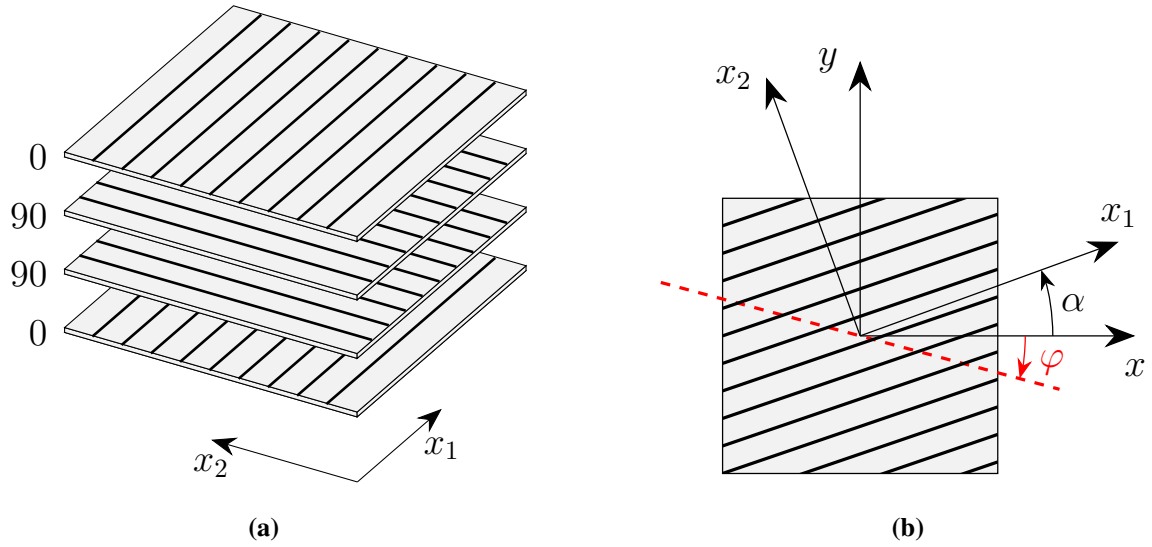


Figure 10: F-TC: a) symmetric cross-ply lamination scheme for the face sheet, b) α is the angle between the principal laminate directions x_1, x_2 and the global reference frame x, y of the plate; φ is the skew angle of the wrinkle pattern, defined as the angle between the direction orthogonal to the wrinkles and the loading direction.

where \tilde{Q}_{PQ}^p , ($P, Q \in [1, 2, 6]$) are ply-specific reduced stiffness coefficients. It is important to emphasize that angles $\alpha \neq 0^\circ, 90^\circ$ result in a non-zero coefficient a_{16} . This coefficient induces the coupling between the extensional and shear behaviors, ultimately leading to the formation of wrinkles at a skew angle with respect to the direction x of the applied compressive load.

4.3.2. Buckling

The present FEM solution is compared to the closed-form solution proposed by Fagerberg and Zenkert [8], along with the outcomes obtained by Vescovini *et al* in Ref. [31] using the Ritz approach. The present FEM and the Ritz solutions adopt both a FSDT model with unitary shear correction factor (ED_{10}) for the face sheets. A refined kinematics is employed for the thick core, with a fifth-order expansion for the in-plane displacement and a fourth-order transverse displacement (ED_{54}). The resulting SGUF model FSDT/ ED_{54} has been demonstrated to yield very accurate solutions for the present case [31]. The in-plane domain is discretized with a regular mesh of square QC4 elements with a side length of 0.5 mm. The mesh thus comprises a total of 7500 elements.

To facilitate the comparison with the solutions in [8, 31], we define the buckling load as one half of the lowest eigenvalue derived from Eq. (12). This corresponds to the critical load of one face sheet instead of that of the whole sandwich panel. The buckling loads and corresponding skew angles of the wrinkle pattern are plotted in Fig. 11 across a range of values of α within the

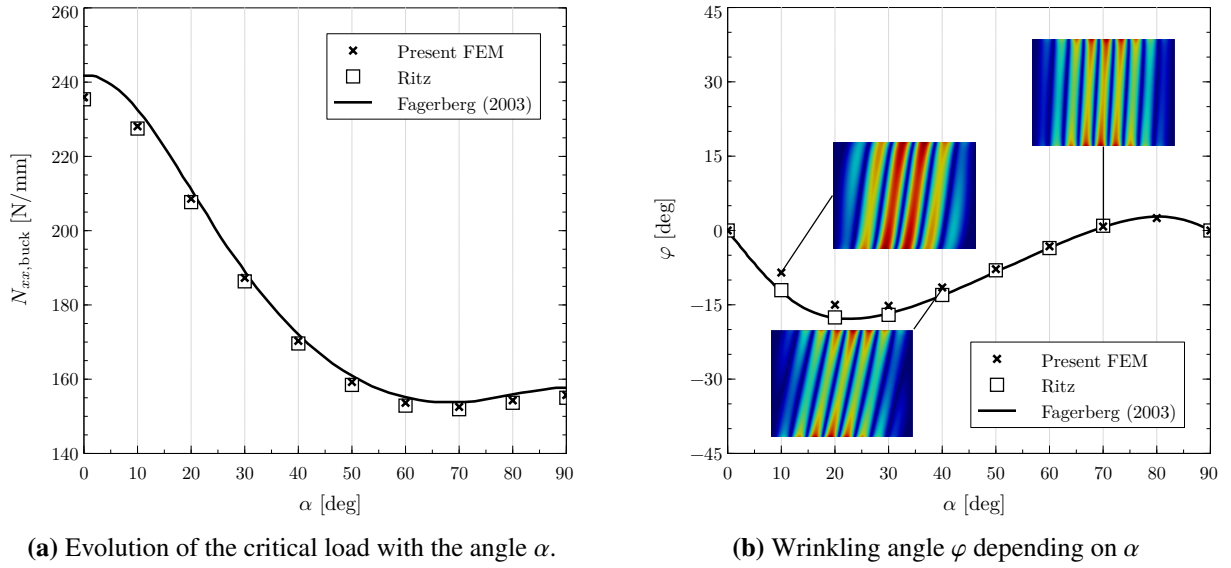


Figure 11: F-TC: Critical loads for one face sheet and corresponding angles of the wrinkling pattern obtained for different orientation angles α of the cross-ply face laminates with respect to the longitudinal x -direction of the uniaxial compression

interval $[0, 90]$. This representation provides a detailed insight into the influence of the angle α on both buckling loads and wrinkle pattern skew angles. Fig. 11b reports also the wrinkling patterns obtained by the present FE solution at the top surface of the panel for the 3 angles $\alpha = 10^\circ, 40^\circ, 70^\circ$. A close agreement is found for the local buckling response of the present FEM with respect to the analytical solution [8] as well as to the Ritz-based results [31]. This successful comparison confirms the capability of the proposed FE approach, to grasp with a simple 2D mesh complex three-dimensional responses characterized by short wave-length deformation patterns.

4.4. Sandwich face sheets wrinkling under transverse load

This case study aims to demonstrate the capability of the present computational approach to compute wrinkling loads for sandwich panels that work in bending, which is the principal structural function of these structures. Indeed, the compression stress state in one of the face sheets may result in local instability, eventually yielding the total failure of the panel. The analysis refers to the three-point bending configuration proposed by Yuan *et al.* [39], and therefore referred to as Yuan-TestCase (Y-TC). It considers a wide sandwich panel made up of two thin and stiff face sheets of Kevlar and a weak and thick PMI foam core (ROHACELL[®] 50). Both face sheet and core materials are assumed to be isotropic. The geometric and elastic properties are summarized in Tab. 7.

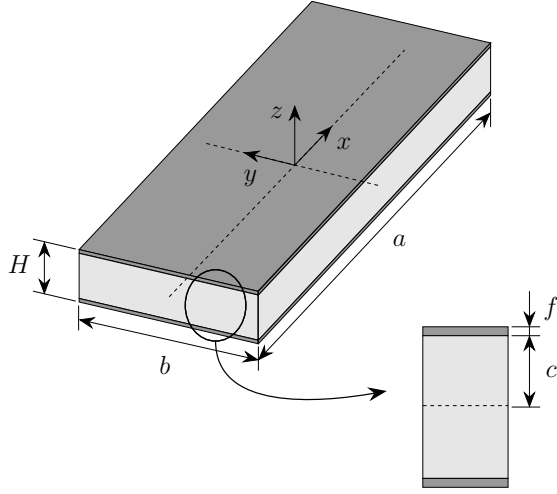


Figure 12: Y-TC: Sandwich beam-plate geometry.

Table 7: Y-TC: Geometric and material data.

$a = 300 \text{ mm}; b = 60 \text{ mm}$		
$f = 0.5; 2c = 19.05 \text{ mm}$		
$H = 20.05 \text{ mm}$		
	ROHACELL [®] 50	Kevlar
E [MPa]	52.5	27400
ν	0.25	0.3
G [MPa]	21	10538.5

With reference to the axes defined in Fig. 12, the sandwich panel is simply-supported at its extremities and subjected to a concentrated force acting at its center ($x = 0$) along the z -direction. Since both loading and boundary conditions exhibit symmetry about the midspan, only the left half-panel is modelled. In contrast to the plane stress assumption underlying the beam model of [39], plane strain assumption is here invoked to confine the response to the (x, z) -plane. As already done in Sec. 4.2, this is realized by constraining $u_y(x, y, z) = 0$. The typically three-dimensional boundary conditions of the three-point bending test are reproduced in a very straightforward manner within the present SGUF modelling: in fact, by virtue of the thickness functions defined by Legendre polynomials, each node of the 2D FE mesh has DOF corresponding to the displacements at the outer surfaces of the panel. The roller boundary condition can thus be accurately reproduced by constraining the transverse displacement at the panel's bottom surface and at specific locations along the x -coordinate, as illustrated in Fig. 13. The boundary conditions applied to the left half-panel are thus

$$u_y(x, y, z) = u_x(0, y, z) = u_z(-a/2, y, -H/2) = 0 \quad (28)$$

and the load is introduced as

$$\int_{-b/2}^{b/2} P_z(x=0, y, z=H/2) dy = -P \quad (29)$$

The sandwich response is evaluated by means of SGUF models adopting four different kinematics for the core, namely ED7, ED₃₂, ED₁₂ and FSDT. The face sheets are always modelled according to FSDT. The sandwich model FSDT/ED₃₂ is close to that employed in [39], namely the EHSAPT

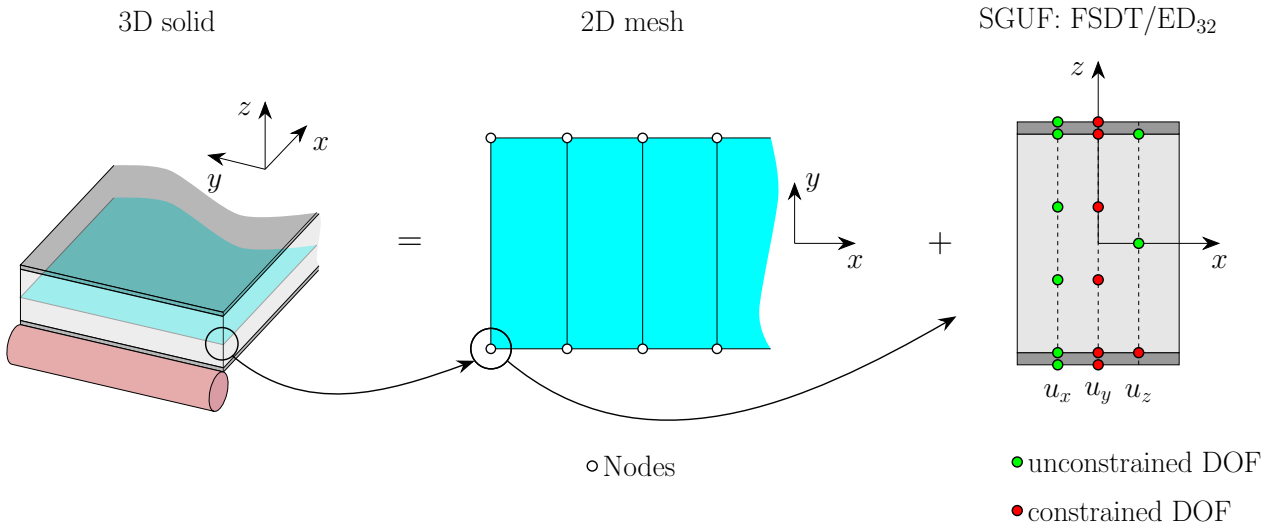


Figure 13: Y-TC: Constraints of the present 2D plate FEM reproducing the roller boundary condition of the three-point bending test and the plane strain condition in the (xz) -plane.

of Phan *et al* [42]. The ED₁₂ kinematics is an enrichment of the FSDT towards the consistent inclusion of the transverse normal deformation.

The FE mesh used for the SGUF models comprises 340 linear elements along the x -direction of the half-panel (only one element is used along the width direction). For the sake of comparison, a 2D plane strain elasticity FE solution obtained with the commercial software package Abaqus is also considered for comparison. In this elasticity model, 4 and 15 elements are stacked along the thickness of the face sheets and the core, respectively. To properly describe the steep gradients in the proximity of the concentrated load, the mesh of the SGUF model and of the Abaqus model is progressively refined towards the symmetry axis by means of a bias factor (bf) of 50. The resulting 2D mesh of the plane strain Abaqus model is illustrated in Fig. 14.

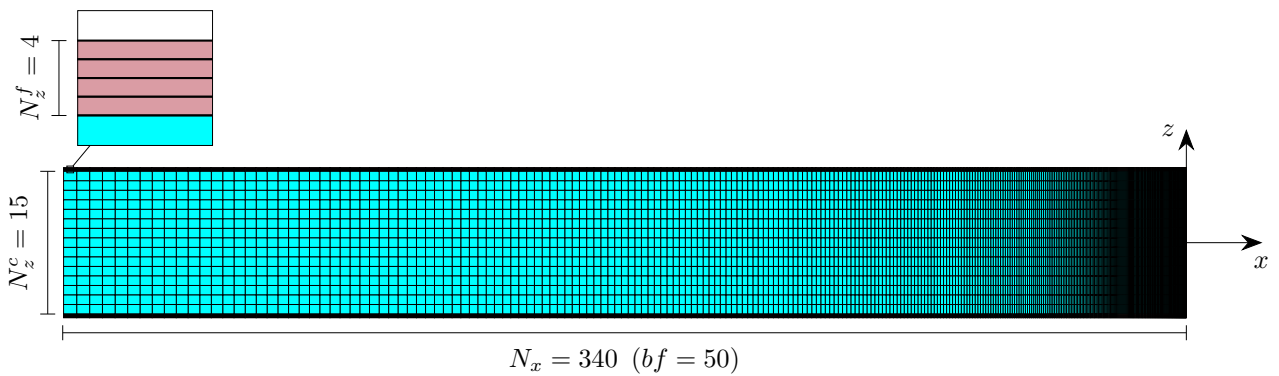


Figure 14: Y-TC: FE model in Abaqus.

4.4.1. Pre-buckling

A first step is required to define the initial stress state, which is achieved by the performing a linear static analysis for the three-point bending configuration. Fig. 15 reports the applied load against the transverse displacement of the midpoint at the top surface, i.e., the point ($x = 0, z = H/2$) of application of the force. Results of the geometrically linear EHSAPT model reported in [39] and the ones obtained with the commercial software Abaqus are included for comparison. Since the analysis is linear elastic, the displacement is obviously proportional to the applied load. A good agreement is found between Abaqus and all SGUF models that retain the transverse compressibility of the core: the sandwich model FSDT/FSDT displays an excessively stiff response because the local indentation of the core under the applied force cannot be grasped. On the other hand, the EHSAPT solution is less stiff due to the plane stress assumption adopted for the beam FEM developed in [39].

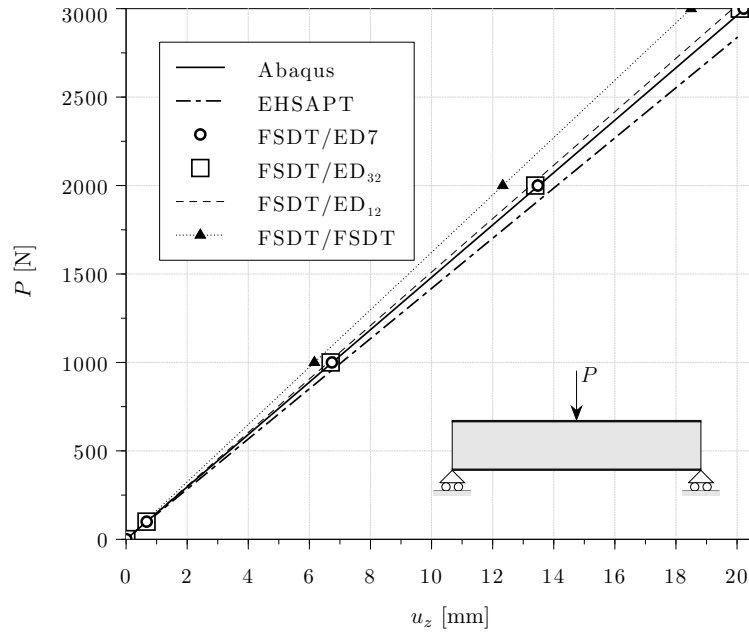


Figure 15: Y-TC: Transverse displacement u_z at sandwich panel midspan for different values of transversal load P .

Fig. 16 shows the distributions of the in-plane axial stress σ_{xx} and the transverse normal stress σ_{zz} across the core at the symmetry plane ($x = 0$) and for a load $P = -1300$ N. These distributions confirm the quasi-3D accuracy of the FSDT/ED7 model, which provides practically identical results compared to the solid FEM of Abaqus that is taken as reference. It is also obvious that the FSDT/FSDT model is limited to a global bending response of the sandwich, it cannot grasp the local bending of the face sheets that come along the indentation occurring due to the concentrated

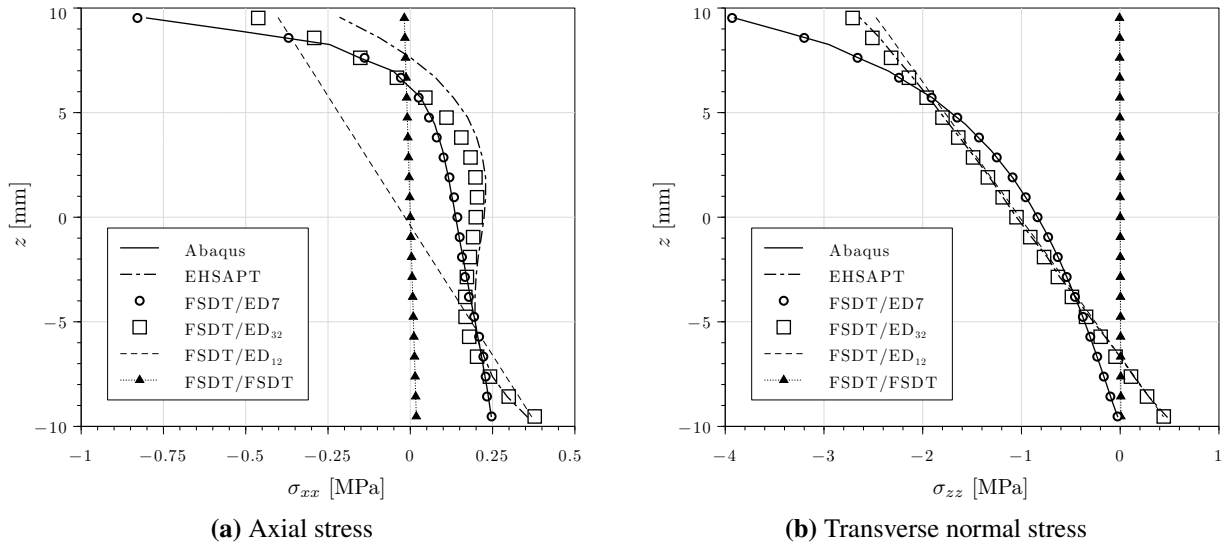


Figure 16: Y-TC: Stress distributions in the core at $x = 0$: a) axial stress, b) transverse normal stress.

force. It is worth emphasizing that very low compressive stresses are predicted by the FSDT/FSDT model on the compressed portion of the sandwich section. This is in contrast with the strongly nonlinear distributions $\sigma_{xx}(x = 0, z)$ predicted by core models that allow the transverse normal deformation, in which only a small region close to the top face sheet is subjected to high compressive axial stresses. The FSDT/ED₁₂ model is shown to improve upon the FSDT by introducing a linear transverse normal stress (Fig. 16b). The effect of the transverse normal strain ϵ_{zz} and the consistent resolution of the Poisson effect can be appreciated in the slight shift of the neutral axis towards the region of the section subjected to tensile stresses, see Fig. 16a. It is also interesting to notice that the results of the model FSDT/ED₃₂ agree well with those obtained in [39] with the geometrically linear analysis with EHSAPT, in particular an identical distribution of the transverse normal stress can be appreciated in Fig. 16b. The small discrepancy observed in Fig. 16a can be due to the already mentioned difference between the beam (plane stress) and wide plate (plane strain) assumptions. However, since the discrepancy is localized at the top face sheet directly under the applied concentrated force, it is more likely that the difference be due to the different mesh refinement, or to the different kinematic model used for the face sheet: EHSAPT adopts in fact the CLT kinematics for the face sheets, and the disregard of the transverse shear effects may yield some inaccuracies in presence of such extremely localized responses.

The axial stress distribution across the face sheets, shaded in gray, is plotted in Fig. 17. It is important to detail out these distributions because these will mainly affect the results of the subse-

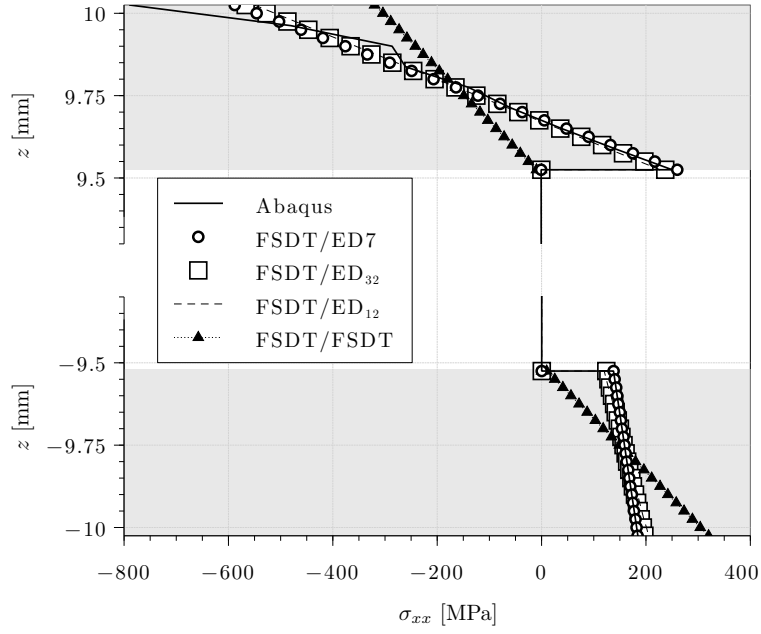


Figure 17: Y-TC: Axial stress distribution across the face sheets thickness at $x = 0$.

quent buckling analysis. The bottom face sheet works entirely in tension as a consequence of the global sandwich bending response. However, the top face sheet undergoes a local bending due to the indentation: only the top portion of the face sheet is subjected to compressive stress, while the bottom portion of the face sheet results to carry tensile axial stresses. As already pointed out, the FSDT/FSDT model is not capable to represent the indentation and, therefore, the local bending of the top face sheet.

4.4.2. Buckling

The second analysis step consists in the solution of the eigenvalue problem Eq. (12), in which the initial stress state is obtained from the previously discussed linear static analysis of a three-point bending problem under the action of a unit force $P = -1$ N acting downwards.

Table 8: Y-TC: First three buckling loads of the sandwich panel in the three-point bending configuration.

Mode	Abaqus	FSDT/ED7 (28)	FSDT/ED ₃₂ (15)	FSDT/ED ₁₂ (11)	FSDT/FSDT (9)
1	-2264.2	-2248.2	-2359.2	-2431.1	-9.3e+12
2	2326.3	2283.3	2402.6	2519.7	-8.0e+14
3	-2464.3	-2453.0	-2582.5	-2692.5	-2.5e+15

Values in parentheses indicate the number of nodal DOF of the model.

The buckling loads for the first 3 modes are listed in Tab. 8 in the order of increasing absolute

value of the eigenvalue. The number of nodal DOFs is also included to provide a qualitative estimation of the computational effort associated with each SGUF model. In order to provide a physical interpretation of the numerical values of Tab. 8, the buckled shapes of the first 2 modes are shown in Fig. 18.

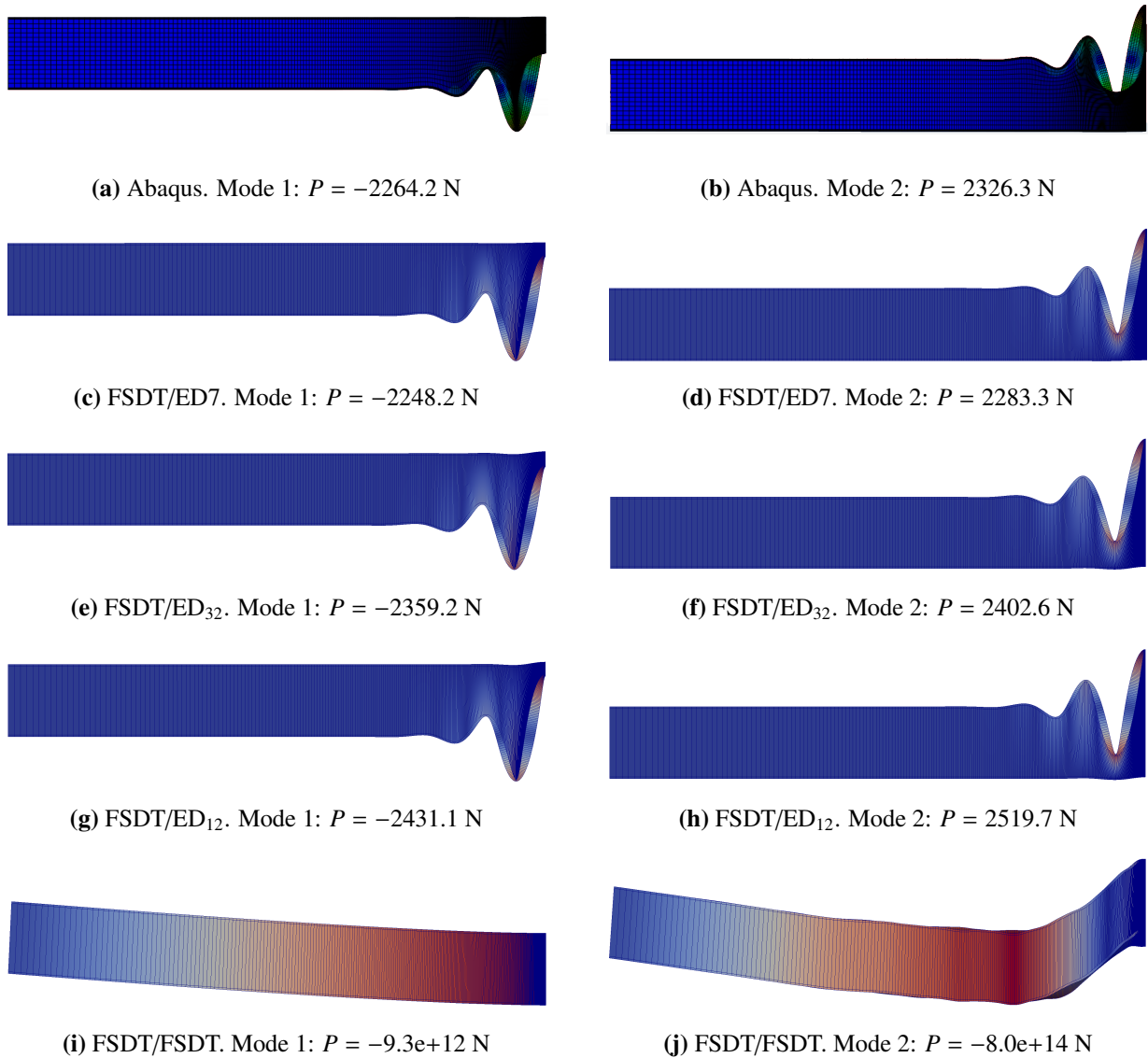


Figure 18: Y-TC: Buckled shapes of the sandwich panel in the three-point bending configuration for the first two buckling modes. Influence of the SGUF model on buckling pattern.

At first, it is obvious that the wrinkling modes cannot be grasped unless the kinematic model adopted for the core allows for its compressibility: results for the FSDT/FSDT model are completely meaningless.

Further, it is remarked that the first buckling mode is associated to a negative eigenvalue, irre-

spective of the model. Looking at Fig. 18a, this mode is shown to correspond to a local instability (wrinkling) of the bottom face sheet – i.e., this wrinkling mode would occur if the sandwich was loaded with a force acting upwards. The reason for this is to be found in the local axial stress distributions obtained from the pre-buckling analysis and reported in Fig. 17. In fact, multiplying by -1 the initial stress state, the bottom skin would buckle first because it results to be entirely under compression. In contrast, the top face sheet is seen to be subjected to axial stresses that are partially in tension and partially in compression due to the local bending. Therefore, a higher absolute value of the eigenvalue is required for the wrinkling of the top face sheet. Indeed, the wrinkling of the top face sheet is associated to a positive eigenvalue and corresponds to the second mode.

Finally, it is noticed the very good agreement between the most refined FSDT/ED7 SGUF model and the quasi-3D solution provided by Abaqus in terms of both, the wrinkling load (a difference of less of 0.2% is obtained) and the modal shape.

4.5. Symmetric sandwich panels under combined in-plane loading

The final case study aims to demonstrate the capability of the proposed approach in addressing buckling under combined in-plane compressive and shear loading. Sandwich panels typical of modern aircraft structures are here considered, in particular those characterizing the Elixir aircraft as referenced in [13, 43]. Specifically, a simply-supported square sandwich plate is investigated, whose geometric and material properties are detailed out in Tab. 9. The layup of the sandwich plate is symmetric and defined in Tab. 10.

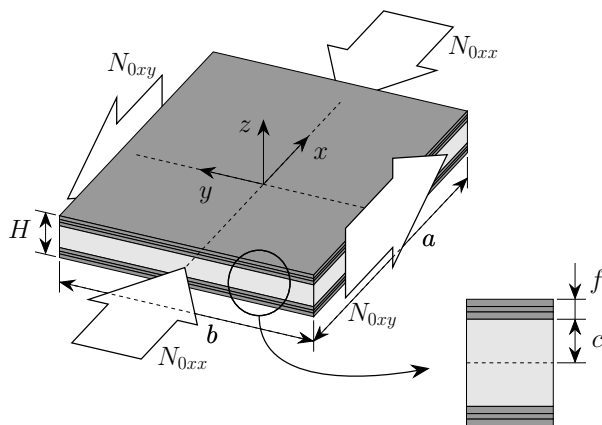


Figure 19: DC-TC: Sandwich plate geometry.

Table 9: DC-TC: Geometric and material data.

$a = b = 260 \text{ mm}, f = 0.61 \text{ mm}$				
	Fabric	UniDir	Foam	Honeycomb
E_1 [MPa]	55000	120000	50	0.5
E_2 [MPa]	55000	10000	50	0.5
E_3 [MPa]	10000	10000	50	140
ν_{12}	0.04	0.3	0.3	0.9
ν_{13}	0.3	0.3	0.3	0.01
ν_{23}	0.3	0.5	0.3	0.01
G_{12} [MPa]	4000	4000	30	1
G_{13} [MPa]	4000	4000	30	40
G_{23} [MPa]	4000	3300	30	25

Table 10: DC-TC: Sandwich layup.

Ply no.	1	2	3	4	5	6	7
h [mm]	0.224	0.162	0.224	$\{0.01, 0.02, \dots, 0.2\} a$	0.224	0.162	0.224
θ [deg]	45	0	45	0	45	0	45
Material	Fabric	Unidir	Fabric	Foam/Honeycomb	Fabric	UniDir	Fabric

Various sandwich configurations are explored, which involve variations in core materials (foam or honeycomb) and core thickness, ranging from thin to very thick. Given that all the results showcased in this section are novel, we shall henceforth denote this case study as Di Cara-TestCase (DC-TC).

4.6. Pre-buckling

The initial strain field described by Eq. (26) is enhanced to incorporate the contribution arising from the imposed shear stress resultant N_{0xy} , which is added to the compressive stress N_{0xx} . Consequently, the initial strain field under this combined in-plane loading is as follows:

$$\begin{aligned}
\epsilon_{0xx} &= a_{11} N_{0xx} + a_{13} N_{0xy} \\
\epsilon_{0yy} &= a_{12} N_{0xx} + a_{23} N_{0xy} \\
\epsilon_{0xy} &= a_{16} N_{0xx} + a_{22} N_{0xy}
\end{aligned} \tag{30}$$

The resulting initial stress field is obtained in the same manner as previously, employing the reduced constitutive law as presented in Eq. (27). It is worth noting that the introduction of in-plane shear loads leads to the occurrence of a wrinkle pattern at a skewed angle with respect to the principal directions, regardless of the lamination scheme.

4.7. Buckling

A first analysis investigates the interaction between shear and compression loading for a rather thick panel with a foam core whose thickness is 15% of the plate length, which corresponds to a total thickness $H = 40.22$ mm. A converged mesh consisting of 100×100 QC4 elements is used. Indeed, the moderate length-to-thickness ratio of the panel and the orthotropic composite face sheets subjected to the combined shear-compression loading give rise to a complex wrinkle pattern, demanding a substantial number of elements to achieve a precise representation.

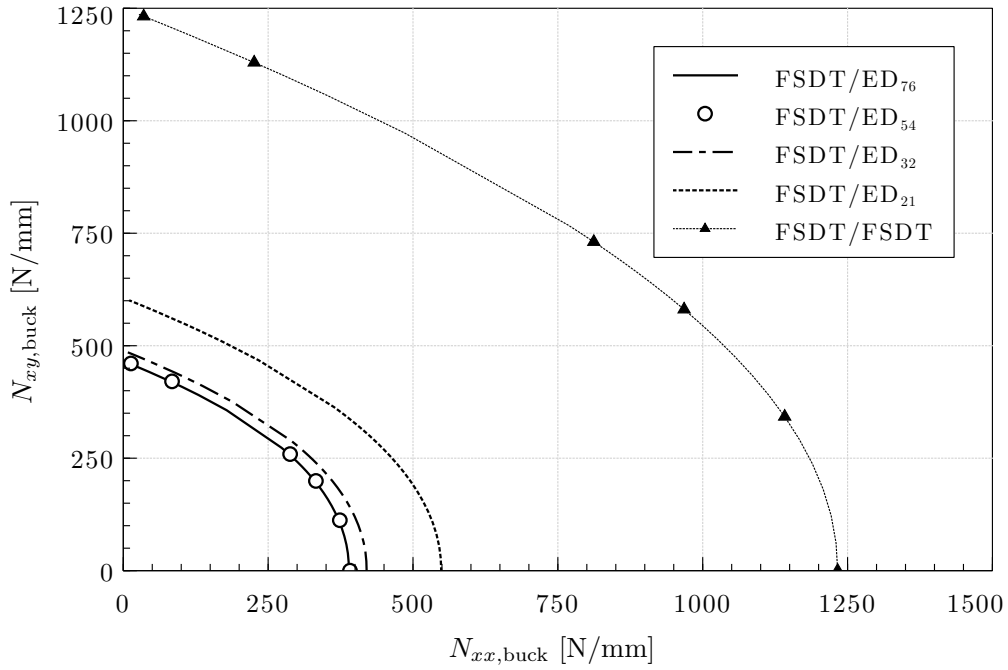


Figure 20: DC-TC: Interaction curves of a sandwich panel with a foam core subjected to combined in-plane shear-compression loading.

The composite face sheets are modelled according to FSDT whilst different models are assessed for the core, namely ED_{21} , ED_{32} , ED_{54} and ED_{76} . The interaction curve obtained for the different core models is illustrated in Fig. 20.

It is observed that a low order model for the core layer significantly overestimates the load-bearing capacity of the sandwich structure. Therefore, a refined kinematics is required to attain an accurate prediction of the buckling load. The results show that the high-order model ED_{54} is required to properly resolve the local wrinkling instabilities. These results are being introduced for the first time in the context of the variable kinematics FE approach, providing evidence of its capability to effectively handle complex loading conditions that involve both shear and compression simultaneously.

The second analysis delves into the transition from global to local instabilities. This shift in the buckling mechanism is initiated by increasing the core's thickness [44]. In fact, augmenting the core layer's thickness enhances the structure's resistance to global buckling. However, the increase of the core thickness redirects the challenge toward local instabilities in the face sheets. Global buckling and face sheet wrinkling appear thus as competing failure mechanisms that must be well identified for a rational sandwich design. The proposed numerical approach actually allows to investigate both

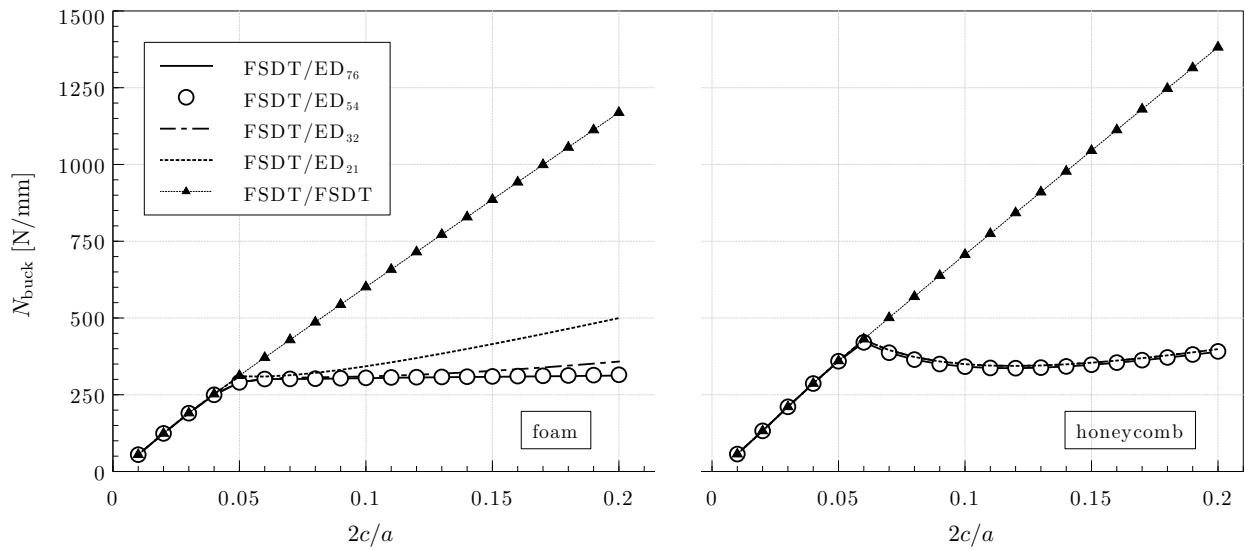


Figure 21: DC-TC: Transition curves of a sandwich panel subjected to combined shear-compression loading condition with $N_{0xy}/N_{0xx} = 0.75$: foam core (left), honeycomb core (right).

buckling mechanisms within a unique modeling framework based on a simple 2D FE mesh.

The same mesh of the previous analysis is retained and the previous SGUF models are used with FSDT for the face sheets and different kinematic models for the core. The critical buckling load per unit length is plotted in Fig. 21 as a function of the ratio between the core thickness and the plate length, denoted as $2c/a$. The analysis is carried out for both foam and honeycomb cores. The loading ratio N_{0xy}/N_{0xx} for this analysis has been set to 0.75.

For low core thickness, the critical buckling mechanisms is the global one, and the buckling loads linearly increase as the core thickness increases because the overall bending rigidity of the panel is enhanced. At a certain threshold value of the core thickness, however, the critical buckling mechanism switches to local wrinkling. The threshold core thickness is shown to depend on the mechanical properties of the core. At a first glance, it is immediate to see in Fig. 21 that, as the FSDT model does not account for the compressibility of the core layer, it fails to detect any transition from global to local buckling mechanisms, irrespective of the core properties. High-order models for the core are again required to grasp the global-local transition. In the wrinkling regime, it is interesting to note the different influence of the core thickness on the critical load of the foam and the honeycomb cores. Fig. 21 shows that increasing the foam core thickness comes along a slight increase of the buckling load, whereas increasing the thickness of the honeycomb core produces at first a decrease of the critical load. An explanation of this phenomenon may be attempted by

analysing the results obtained with different kinematic models used for the core. It is shown that converged results for the honeycomb core are obtained with the ED_{21} model (Fig. 21, right), whereas the refined model ED_{54} is required for resolving the wrinkling of the foam core (Fig. 21, left). This suggests that the transverse shear deformation plays a more relevant role in the foam core than in the honeycomb core [12, 31]. In fact, the negligible in-plane stiffness of the honeycomb structure induces a nearly pure extensional deformation (symmetric wrinkling mode), in which the transverse shear plays a negligibly small role. On the contrary, the isotropic foam core induces an antisymmetric wrinkling mode which is heavily influenced by the transverse shear rigidity. Since the thickness enhances the transverse shear stiffness, the wrinkling load of the foam core panel increases with the core thickness. However, the transverse normal stiffness is independent of the core thickness, thus the initial reduction of the critical load occurs for honeycomb core thicknesses directly above the threshold value.

5. Conclusions

This paper has extended the variable kinematics approach, referred to as Sublaminar Generalized Unified Formulation (SGUF), towards the linearized buckling analysis in the framework of the Finite Element Method (FEM). The variable kinematics geometric stiffness matrix is built for membrane loads by referring to von Kármán approximation and the classical bifurcation buckling problem is solved by means of eigenvalue analysis. A number of representative case studies have been addressed for displaying the accuracy and flexibility of the proposed SGUF-FEM tool: global buckling of symmetric cross-ply laminates, the transition from global to local buckling of sandwich panels under different loading conditions and depending on characteristic geometric and material parameters of the sandwich section, including anisotropic face sheets, orthotropic as well as isotropic cores. The results illustrate the capability of this approach to grasp complex three-dimensional failure mechanisms such as the wrinkling of the face sheets within a simple 2D FE mesh. This advantage sets the proposed method apart from currently available commercial Finite Element packages, and it appears as particularly useful in the context of preliminary design phases.

Further developments of the SGUF-FEM tool shall be directed towards the inclusion of material failure and delamination initiation criteria. Also, progressive failure analysis arises as a required development in view of advanced structural designs. The extension towards geometric as well material non-linearities shall in particular allow to grasp post-buckling responses, global-local buck-

ling interactions and delamination propagation. The promising advantages of functionally graded sandwich structures as efficient load carrying thermal barriers or lightweight ballistic panels further suggest to extend the presented SGUF-FEM tool towards plies with continuously varying material parameters, thermal effects and dynamic response.

References

- [1] B. Castanié, C. Bouvet, and M. Ginot. Review of composite sandwich structure in aeronautic applications. *Compos. C*, 1:100004, 2020.
- [2] J. R. Vinson. *The Behavior of Sandwich Structures of Isotropic and Composite Materials*. Technomic Publishing Co., Lancaster, 1999.
- [3] L. A. Carlsson and G. A. Kardomateas. *Structural and Failure Mechanics of Sandwich Composites*. Springer, Berlin, 2011.
- [4] H. G. Allen. *Analysis and Design of Structural Sandwich Panels*. Pergamon Press, 1969.
- [5] R. P. Ley, W. Lin, and U. Mbanefo. Facesheet Wrinkling in Sandwich Structures. Technical Report NASA/CR-1999-208994, NASA, 1999.
- [6] L. Fagerberg. The effect of local bending stiffness on the wrinkling of sandwich panels. *Proc. Inst. Mech. Eng.*, 217(2):111–119, 2003. doi:10.1243/147509003321921355.
- [7] L. Fagerberg. Wrinkling and Compression Failure Transition in Sandwich Panels. *J. Sandw. Struct. Mater.*, 6(2):129–144, 2004. doi:10.1177/1099636204030475.
- [8] L. Fagerberg and D. Zenkert. Effects of Anisotropy and Multiaxial Loading on the Wrinkling of Sandwich Panels. *J. Sandw. Struct. Mater.*, 7(3):177–194, 2005. doi:10.1177/109963205048525.
- [9] L. Fagerberg and D. Zenkert. Imperfection-induced Wrinkling Material Failure in Sandwich Panels. *J. Sandw. Struct. Mater.*, 7(3):195–219, 2005. doi:10.1177/1099636205048526.
- [10] A. Gutierrez and J. Webber. Flexural wrinkling of honeycomb sandwich beams with laminated faces. *Int. J. Solids Struct.*, 16(7):645–651, 1980. doi:10.1016/0020-7683(80)90023-2.

- [11] B. Zalewski, W. Dial, and B. Bednarczyk. Methods for Assessing Honeycomb Sandwich Panel Wrinkling Failures. Technical Report NASA/TM-2012-217697, NASA, 2012.
- [12] M. D’Ottavio and O. Polit. Linearized global and local buckling analysis of sandwich struts with a refined quasi-3D model. *Acta Mech.*, 226(1):81–101, 2015. doi:10.1007/s00707-014-1169-2.
- [13] M. Ginot, M. D’Ottavio, O. Polit, C. Bouvet, and B. Castanié. Benchmark of wrinkling formulae and methods for pre-sizing of aircraft lightweight sandwich structures. *Compos. Struct.*, 273:114387, 2021. doi:10.1016/j.compstruct.2021.114387.
- [14] W. Ji and A. M. Waas. Global and Local Buckling of a Sandwich Beam. *J. Eng. Mech.*, 133(2):230–237, 2007. doi:10.1061/(ASCE)0733-9399(2007)133:2(230).
- [15] W. Ji and A. M. Waas. Wrinkling and Edge Buckling in Orthotropic Sandwich Beams. *J. Eng. Mech.*, 134(6):455–461, 2008. doi:10.1061/(ASCE)0733-9399(2008)134:6(455).
- [16] W. Ji and A. M. Waas. 2D elastic analysis of the sandwich panel buckling problem: benchmark solutions and accurate finite element formulations. *Z. Angew. Math. Phys.*, 61(5):897–917, 2010. doi:10.1007/s00033-009-0041-z.
- [17] A. S. Benson and J. Mayers. General instability and face wrinkling of sandwich plates – Unified theory and applications. *AIAA J.*, 5:729–739, 1967.
- [18] B. Hadi and F. Matthews. Development of Benson–Mayers theory on the wrinkling of anisotropic sandwich panels. *Compos. Struct.*, 49(4):425–434, 2000. doi:10.1016/S0263-8223(00)00077-5.
- [19] L. Léotoing, S. Drapier, and A. Vautrin. First applications of a novel unified model for global and local buckling of sandwich columns. *Eur. J. Mech. A Solids*, 21(4):683–701, 2002. doi:10.1016/S0997-7538(02)01229-9.
- [20] M.-A. Douville and P. Le Grogneq. Exact analytical solutions for the local and global buckling of sandwich beam-columns under various loadings. *Int. J. Solids Struct.*, 50:2597–2609, 2013.

- [21] L. Léotoing, S. Drapier, and A. Vautrin. Nonlinear interaction of geometrical and material properties in sandwich beam instabilities. *Int. J. Solids Struct.*, 39(13-14):3717–3739, 2002. doi:10.1016/S0020-7683(02)00181-6.
- [22] M. A. Wadee, S. Yiatros, and M. Theofanous. Comparative studies of localized buckling in sandwich struts with different core bending models. *Int. J. Non Linear Mech.*, 45(2):111–120, 2010. doi:10.1016/j.ijnonlinmec.2009.10.001.
- [23] E. Carrera, M. Cinefra, M. Petrolo, and E. Zappino. *Finite Element Analysis of Structures through Unified Formulation*. John Wiley & Sons, Ltd, Chichester, UK, 2014.
- [24] L. Demasi. Partially Layer Wise advanced Zig Zag and HSDT models based on the Generalized Unified Formulation. *Engng. Struct.*, 53:63–91, 2013.
- [25] M. D’Ottavio. A Sublaminar Generalized Unified Formulation for the analysis of composite structures. *Compos. Struct.*, 142:187–199, 2016. doi:10.1016/j.compstruct.2016.01.087.
- [26] A. Pagani and E. Carrera. Large-deflection and post-buckling analyses of laminated composite beams by Carrera Unified Formulation. *Compos. Struct.*, 170:40–52, 2017. doi:10.1016/j.compstruct.2017.03.008.
- [27] A. Pagani and E. Carrera. Unified formulation of geometrically nonlinear refined beam theories. *Mech. Adv. Mater. Struct.*, 25(1):15–31, 2018. doi:10.1080/15376494.2016.1232458.
- [28] A. Pagani, E. Daneshkhah, X. Xu, and E. Carrera. Evaluation of geometrically nonlinear terms in the large-deflection and post-buckling analysis of isotropic rectangular plates. *Int. J. Non Linear Mech.*, 121:103461, 2020. doi:10.1016/j.ijnonlinmec.2020.103461.
- [29] Y. Hui, G. Giunta, G. De Pietro, S. Belouettar, E. Carrera, Q. Huang, X. Liu and H. Hu. A geometrically nonlinear analysis through hierarchical one-dimensional modelling of sandwich beam structures. *Acta Mech.*, 234(1):67–83, 2023. doi:10.1007/s00707-022-03194-7.
- [30] M. D’Ottavio, O. Polit, W. Ji, and A. M. Waas. Benchmark solutions and assessment of variable kinematics models for global and local buckling of sandwich struts. *Compos. Struct.*, 156:125–134, 2016. doi:10.1016/j.compstruct.2016.01.019.

- [31] R. Vescovini, M. D’Ottavio, L. Dozio, and O. Polit. Buckling and wrinkling of anisotropic sandwich plates. *Int. J. Eng. Sci.*, 130:136–156, 2018. doi:10.1016/j.ijengsci.2018.05.010.
- [32] G. Di Cara, M. D’Ottavio, T. H. C. Le, and O. Polit. Finite plate elements with variable kinematics based on sublaminar generalized unified formulation. *Mech. Adv. Mater. Struct.*, 30(5):1031–1049, 2023. doi:10.1080/15376494.2022.2126568.
- [33] T. H. C. Le, M. D’Ottavio, P. Vidal, and O. Polit. A new robust quadrilateral four-node variable kinematics plate element for composite structures. *Finite Elem. Anal. Des.*, 133:10–24, 2017. doi:10.1016/j.finel.2017.05.002.
- [34] T. H. C. Le, M. D’Ottavio, P. Vidal, and O. Polit. Robust Displacement and Mixed CUF-Based Four-Node and Eight-Node Quadrilateral Plate Elements. In *Analysis and Modelling of Advanced Structures and Smart Systems. Advanced Structured Materials*, volume 81, pages 89–118. Springer, Singapore, 2018.
- [35] E. N. Dvorkin and K. Bathe. A continuum mechanics based four-node shell element for general non-linear analysis. *Eng. Comput.*, 1(1):77–88, 1984. doi:10.1108/eb023562.
- [36] M. Cinefra, M. D’Ottavio, O. Polit, and E. Carrera. Assessment of MITC plate elements based on CUF with respect to distorted meshes. *Compos. Struct.*, 238:111962, 2020. doi:10.1016/j.compstruct.2020.111962.
- [37] K. Washizu. *Variational Methods in Elasticity and Plasticity*. Elsevier Science & Technology, Amsterdam, 1974.
- [38] A. K. Noor. Stability of multilayered composite plates. *J. Fiber Sci. Technol.*, 8(2):81–89, 1975. doi:10.1016/0015-0568(75)90005-6.
- [39] Z. Yuan, G. A. Kardomateas, and Y. Frostig. Geometric Nonlinearity Effects in the Response of Sandwich Wide Panels. *J. Appl. Mech.*, 83(9):091008, 2016. doi:10.1115/1.4033651.
- [40] M. D’Ottavio and E. Carrera. Variable-kinematics approach for linearized buckling analysis of laminated plates and shells. *AIAA Journal*, 48(9):1987–1996, 2010. doi:10.2514/1.J050203.

- [41] E. Carrera and S. Brischetto. Analysis of thickness locking in classical, refined and mixed theories for layered shells. *Compos. Struct.*, 85(1):83–90, 2008. doi:10.1016/j.compstruct.2007.10.009.
- [42] C. N. Phan, Y. Frostig, and G. A. Kardomateas. Analysis of Sandwich Beams With a Compliant Core and With In-Plane Rigidity-Extended High-Order Sandwich Panel Theory Versus Elasticity. *J. Appl. Mech.*, 79(4):041001, 2012. doi:10.1115/1.4005550.
- [43] M. Ginot, C. Bouvet, B. Castanié, M. D’Ottavio, J. Serra, and N. Mahuet. Local buckling on large sandwich panels applied to light aviation: experimental and computation dialogue. *Int. J. Solids Struct.*, 268:112170, 2023. doi:10.1016/j.ijsolstr.2023.112170.
- [44] C. A. Rose, D. F. Moore, N. F. Knight, Jr., and C. C. Rankin. Finite element modeling of the buckling response of sandwich panels. In *43rd AIAA/ASME/ASCE/AHS/ASC Structures, Structural Dynamics, and Materials Conference*, page 1517, 2002.